ADVANCED LASER DIAGNOSTICS DEVELOPMENT FOR STEREOSCOPIC IMAGING OF GASEOUS HIGH SPEED FLOWS

A Thesis

by

FENG PAN

Submitted to the Office of Graduate and Professional Studies of
Texas A&M University
in partial fulfillment of the requirements for the degree of

MASTER OF SCIENCE

Chair of Committee,	Simon W. North
Committee Members,	Rodney D. W. Bowersox
	Dong Hee Son
Head of Department,	Simon W. North

May 2016

Major Subject: Chemistry

ABSTRACT

The coupled interactions between turbulent flow and thermal non-equilibrium (TNE) are physical and chemical processes with significant implications in turbulent heat transfer, fluid mixing, and fluid transport associated with high-speed vehicles and propulsion systems. Understanding the coupling mechanism allows one to utilize energy exchange for intelligent control of basic fluid dynamics processes. However, the elucidation of this mechanism necessitates quantifying the correlation of velocity fluctuations and scalar distributions. Thus, the development of reliable diagnostic techniques capable of simultaneous measurement of such quantities is necessary. Since turbulence is intrinsically three-dimensional, the measurement of the three-component velocity is imperative.

The goal of this research is to develop a laser-based diagnostic technique as a non-intrusive approach to simultaneously measure three-component velocity and scalar fields to understand the coupling between turbulence and thermal non-equilibrium. It extends our recently developed Vibrationally Excited Nitric Oxide Monitoring (VENOM) method, which enables (1) the simultaneous measurement of 3D-velocity and planar temperature in cold, high-speed flows and (2) investigation of mean and instantaneous fluctuations in velocity and temperature. Experimental measurements of velocity and temperature across an oblique shock using the VENOM technique result in mean values within 21 m/s for the three components of velocity and 20 K for planar temperature when compared to oblique shock calculations. This extended stereoscopic VENOM system is expected to push forward the development of next-generation VENOM, *i.e.*, dual-plane stereoscopic VENOM, for unprecedented characterization of fluid elements in three dimensions.

ACKNOWLEDGEMENTS

Firstly, I would like to thank my advisor, Dr. Simon North, for his mentorship in the past three years. His patience for mentoring students, passion for science, highly skilled communication ability, wonderful teaching capability, along with energetic life style, have been stimulating me to make improvements on every aspect of my life. These positive characteristics are truly influencing me in terms of what abilities I should possess when I am pursuing an academic career.

Secondly, I would like to show my gratitude to Rodrigo Sanchez-Gonzalez for leading me to the field of laser diagnostics development. I value the experiments we have done together and am grateful for what he taught me, such as the laser beam alignment, data acquisition and analysis programming. Instead of directly showing me answers, he always encouraged me to find those answers by myself. I remember how many times he turned me down by saying “google it and teach yourself” when I really wanted a quick answer from him. However, I really had a lot of fun and benefited from this learning approach, which I think also reshaped my thinking when learning something new. This understanding benefited me a lot when I conducted invisible ink experiments by myself when he left our group. At the same time, I want to thank everyone from the North Group: Niclas West for making scientific nerds jokes on me and himself and helping me with NO LIF scan; and Michelle Warter for sharing the office with me; Wei Wei, Josh Winner and Colin Wallace for their help on my Chem681 seminar practice; Maddie McIlvoy for making fun when we worked together at the wind tunnel; and Kenny Root for his effort to make fuel injector opening times measurements work on the test chamber. In addition, I want to extend many thanks to my colleagues at the National Aerothermochemistry Laboratory. First and foremost, I want to thank Dr. Bowersox for allowing me to “mess around” at the lab and his valuable mentorship on my research. I have really learned a lot by discussing with Dr. Bowersox and those engineers in the field of hypersonic and turbulence transitions studies. Among these colleagues, I would like to thank Brianne McManamen for useful discussion on the cross-correlation analysis technique and for sharing those four PLIF laser systems with me; also Ian Neel for the discussion on fluorescence images

processing using PIV program packet, which I believe will help us reap some research fruits by revolutionizing MTV images processing techniques.

Additionally, I want to show unparalleled gratitude towards my parents for letting me study abroad and pursue my interest. Although they were not highly educated, their wisdom and foresight were shown in a lot of scenarios, such as encouraging me to attend one of the top high schools in China, which is far from our home, to obtain a better education, and pushing me to live and think independently instead of clinging to their thoughts. The way they raised me up made me develop independence from an early age and become very mature compared with my peers. They have never worried about whether or not I made mistakes during this process. Their wisdom has helped me develop the characteristics of perseverance, patience, optimism and resilience. At the same time, I would thank my sister for making fun and cheering me up when I was in low spirits. I really appreciate that she likes to share her funny stories with me.

Lastly, I would like to thank friends I made at Texas A&M. I really fell in love with Aggieland, Home of the 12th Man. The faculty and staff working in Department of Chemistry are fantastic. In particular, I would like to thank our administrative assistant, Monica Gonzalez, for her wonderful job helping us place numerous purchase orders and make our research go smoothly. In addition, I want to thank William Seward working in Machine Shop for his sophisticated skills and amazing work, and Tim Pehl working in Electronic Shop for solving our electronic problems of our facilities and making it possible that we can finally replace pulse valves with fuel injectors.

TABLE OF CONTENTS

Page

Page

LIST OF FIGURES

LIST OF TABLES

1. INTRODUCTION*

1.1 Background and Motivation

Turbulence is a flow condition characterized by fluctuations, irregularity, and chaos as seen in Fig. 1.1. Despite these fluctuations turbulent flow is still governed by the Navier-Stokes equations. In turbulent flow various flow quantities show a random variation at any given point in space and/or time, but statistically distinct average values can be discerned. Other features of turbulence are its diffusivity and multiple length scales. The three important length scale types are the integral length scale, the Taylor microscale, and the Kolmogorov length scale. The integral length scale is indicative of the larger turbulent structures in the flow which contain most of the turbulent kinetic energy. The Kolmogorov scale describes the smallest turbulent structures where viscous effects dominate and dissipate the turbulent energy. The Taylor microscale is a well-defined quantity often used to calculate the Taylor-microscale Reynolds number in direct numerical simulation (DNS) studies. The DNS which can solve the Navier-Stokes equations directly without modeling, has been performed in low-Reynolds number flow fields. However, solving the equations over the requisite time and length scales in realistic flows is intractable, so turbulent flows are necessarily treated stochastically. The typical stochastic treatment is to decompose variables into a mean and fluctuating variables. There are two decomposition methods, Reynolds (time-based) decomposition and Favre (mass-average-based) decomposition [1]. The first decomposition method is:

$$\mu = \bar{\mu} + \mu' \qquad \text{(Eq. 1.1)}$$

Where

$$\bar{\mu} = \frac{1}{T}\int_0^T \mu(t)dt \qquad \text{(Eq. 1.2)}$$

The second decomposition is:

$$\mu = \tilde{\mu} + \mu'' \qquad \text{(Eq. 1.3)}$$

Where

$$\tilde{\mu} = \frac{\overline{\rho\mu}}{\bar{\rho}} = \frac{\int_0^T \rho(t)\mu(t)dt}{\int_0^T \rho(t)dt} \qquad \text{(Eq. 1.4)}$$

* Part of this section is reprinted with permission from "Advanced laser diagnostics development for the characterization of gaseous high speed flows" by Rodrigo Sánchez-González, Ph.D. dissertation, Texas A&M University [7]. Copyright 2012 by Rodrigo Sánchez-González.

For compressible flows, the Favre decomposition is preferred since the averaging equation form is more similar to the original equation than the averaging equation obtained with the Reynolds decomposition. The decomposition variables are inserted back into the governing Navier-Stokes equations, and the equations are averaged. The resulting equations have additional terms, such as the Reynolds stress τ_{ij}^{T} and the turbulent heat flux q_{ij}^{T} shown in Eq. 1.5 and 1.6. This results in a closure problem since there are more terms than there are equations, and thus suitable models for these terms are required for the turbulent flow modeling.

$$\tau_{ij}^{T} = -\overline{\rho u_i'' u_j''} \qquad \text{(Eq. 1.5)}$$

$$q_{ij}^{T} = \overline{\rho h'' u_j''} \qquad \text{(Eq. 1.6)}$$

Fig. 1.1. Colored cigarette smoke undergoing transition from laminar to turbulence state [2].

The turbulent energy cascade is the process of energy passing from the energy-containing range through the inertial subrange, where inertial effects are dominant, to the dissipation range, where viscous effects are dominant. The dissipation range is characterized by small length scales such as the Kolmogorov length scale. This process is shown in Fig. 1.2.

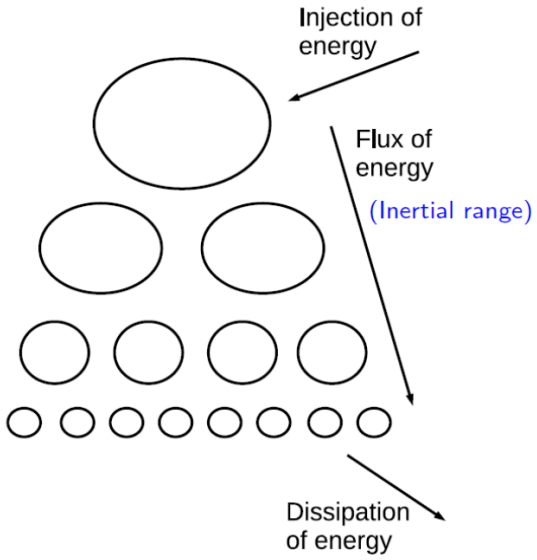

Fig. 1.2. Turbulent energy cascade [3].

Coupled interactions between turbulent flow and thermal non-equilibrium are physical and chemical processes with significant implications in energy flux associated with high-speed vehicles and propulsion systems. Some simple assumptions have been generally used to predict mean flow properties, but have failed to describe in detail flow behavior at a variety of temporal and spatial scales, due to the complication of thermal non-equilibrium phenomena. The turbulent properties of a flow field can be explained by thermodynamic variations across the flow, and therefore accurate modeling of turbulence in high-speed flows requires the coupling between thermal non-equilibrium and basic turbulent processes. However, understanding the coupling necessitates quantifying the correlation of velocity fluctuations and scalar distributions. Thus, the development of reliable diagnostic techniques capable of simultaneous measurement of such quantities is necessary. Since turbulence is intrinsically three-dimensional, the measurement of the three-component velocity is imperative. There are several optical diagnostic techniques that provide simultaneous measurements of one-component or two-component velocity and scalar fields, which in principle could be extended to obtain three components of velocity.

The National Aerothermochemistry Laboratory at Texas A&M University houses numerous state-of-the-art high-speed flow facilities and advanced diagnostics. This

interdisciplinary laboratory has been established to experimentally and theoretically study transitional and turbulent flows, which has resulted in collaborative research between Departments of Aerospace Engineering and Chemistry.

This thesis presents the development of a laser-based diagnostic technique as a non-intrusive approach to gain insight into the coupled interactions between fluid dynamics and molecular transport. This technique addresses the experimental concerns described above and is expected to be not only applied to cold high-speed flows, which is the main focus of the present study, but also to freestream turbulence in high-enthalpy shock tunnels and ablating flows, to which techniques relying on intrusive probes and large particles seeding have been previously applied.

1.2 Research Objectives

The main objectives of the study consist of (1) the further development of the Vibrationally Excited Nitric Oxide Monitoring (VENOM) technique for simultaneous measurement of 3D-velocity and planar temperature in cold high-speed flows using Nitric Oxide Planar Laser Induced Fluorescence (NO PLIF) methods, and (2) investigation of instantaneous fluctuations in velocity and temperature.

All the measurements were conducted using the recently modified pulsed hypersonic facility [4] which enables stereoscopic imaging of the flow field. The stereoscopic VENOM technique represents the first single diagnostic technique capable of simultaneously measuring three-component velocity and planar temperature in a gaseous flow field. This technique is composed of two NO PLIF methods, *i.e.*, three-component Molecular Tagging Velocimetry (MTV) and two-line thermometry, both relying on vibrationally excited NO produced from NO_2 photodissociation or via fluorescence and quenching of electronically excited NO. The two-component MTV using NO generated from NO_2 photodissociation has been demonstrated by Hsu et al. in a underexpanded jet under a variety of quenching conditions [5, 6]. The combination of two-component MTV and two-line thermometry implemented by Sanchez-Gonzalez et al. provided 2D simultaneous measurement of mean and instantaneous fluctuations in velocity and temperature [7-9]. However, the stereoscopic imaging with the use of VENOM approach is not straightforward, and thus requires several considerations: (1) the derivation of 3D displacement vectors from 2D MTV measurements, (2) the thermal effect of nascent NO

rotational thermalization originated from NO_2 photodissociation, (3) energy deposition into the flow via quenching of electronically excited NO. This study addresses these issues and discusses the merits and drawbacks of the two approaches of producing vibrationally excited NO for simultaneous measurement of three-component velocity and planar temperature.

This extended stereoscopic VENOM scheme paves the way for the development of next-generation VENOM, *i.e.*, dual-plane stereoscopic VENOM, for unprecedented characterization of fluid elements in three dimensions. Thus, it will enable the investigation of undocumented physical and chemical processes that couple thermodynamics and fluid dynamics, and hence represents a transformational advance in diagnostics.

1.3 Literature Review

There are numerous experimental studies that provide insight into the coupling of the fluid dynamics and the energy transfer, specifically measurement of velocity and scalar fields. These studies include the measurement of velocity or simultaneous examination of velocity and scalar fields relying on particles tracking or molecular tagging. A brief summary of the molecular tagging velocimetry methods used in gaseous and liquid flow fields was made by Hsu et al, in which both seeded and unseeded techniques are discussed [6]. A variety of techniques capable of simultaneous measurement of one-component or two-component velocity and scalar fields have been reported, which in principle could be extended to obtain three components of velocity [10]. Forkey and Miles employed filtered Rayleigh scattering (FRS) for planar flow visualization and quantitative measurements of velocity, temperature, and density in unseeded gaseous flows [11]. This method, however, shows reduced accuracy at low velocities due to reduced Doppler shifts and low signal-to-noise ratio caused by background scattering and spatial variations in the laser sheet. Exton and Hillard demonstrated the simultaneous measurement of flow velocity, temperature, and pressure via Raman Doppler velocimetry (RDV) [12]. However, apart from suffering from similar reduced inaccuracy at low velocities to FRS technique, this approach relies on signal integration along the laser's path, reducing the potential to perform spatially-resolved measurements. Other methods used to perform simultaneous measurement of velocity and scalar fields involve the combination of techniques such as

particle image velocimetry (PIV) and FRS (PIV/FRS) [13] or planar laser induced fluorescence (PLIF) (PIV/PLIF) [14-19]. However, in high-speed applications, PIV often suffers from non-uniform particle seeding and inaccuracies in tracking velocity across strong gradients [19, 20], in addition to a prohibitive degree of light scattering near surfaces. Hu and Koochesfahani demonstrated simultaneous measurement of two-component velocity and temperature in a fluid, where water-soluble supramolecular complexes were used as tracer molecules [21]. This approach simplifies the experimental set-up with respect to previous PIV/PLIF experiments, but relies on the use of water-soluble molecules and delay times significantly larger than those needed in fast gaseous flow fields applications. Recently, Miles and co-workers have employed femtosecond laser electronic excitation tagging (FLEET) to simultaneously measure velocity and temperature in unseeded flows using a single laser [22]. Although this technique utilizes a simple experimental set-up and is free from seeding particles and possible resulting effects, the temperature measurement relies on the comparison of relatively broader spectral regions, resulting in the complexity associated with using a spectrometer.

Three-component velocity determinations have been demonstrated using stereoscopic PIV [23-25]. As a molecular counterpart of stereoscopic PIV, stereoscopic molecular tagging velocimetry (stereo-MTV) measurements reported by Grünefeld, Koochesfahani and Naqwi demonstrated the advantage of unbiased flow tracking by overcoming the drawbacks of non-uniform particle seeding and disturbance of the flow field caused by stereoscopic PIV [26-28], allowing accurate stereoscopic velocimetry in highly turbulent flow fields [28]. The vibrationally excited nitric oxide monitoring (VENOM) technique previously developed by our group provides a non-intrusive molecular tagging diagnostic method for the simultaneous and instantaneous determination of two components of velocity and temperature in gaseous flow fields [8, 9, 29], where NO (v"=1) serves as a molecular tracer. The use of two “read” lasers in the VENOM technique permits measurements in an extended range of quenching conditions, including air mixtures, and thus in a variety of flow compositions [6]. A grid of NO (v" = 1), generated by either photolysis of NO_2 [6, 8, 9] or more recently by fluorescence and quenching from the A $^2\Sigma^+$state of NO [29], is probed at ~224 nm at different time delays to track the local displacements of the grid. This approach allows the measurement of velocity in higher quenching environments [6] than NO fluorescence MTV [30], since the generated NO (v"

= 1) is depleted only through slow recombination in the case of NO_2 photodissociation VENOM, diffusing and mixing out of the laser probe volume, and slow vibrational relaxation. This configuration also allows one to probe two different rotational states when performing MTV, resulting in the simultaneous measurement of temperature fields [31], by de-warping the second time-delayed grid image back onto the initial image based on the determined local grid displacements [7-9, 29].

1.4 Theoretical Background

1.4.1 Nitric Oxide Laser Induced Fluorescence

Laser Induced Fluorescence (LIF) is a spectroscopic technique that involves the excitation of a molecular target by a beam of laser radiation followed by the detection of the subsequent emission of radiation from the target [32]. LIF is widely used for diagnostic studies due to such advantages over absorption spectroscopy as excellent detection sensitivity, various detection angles, state-specific emission, etc. The high sensitivity of LIF allows the 2D measurements with excellent spatial and temporal resolution by shaping laser beams into sheets, *i.e.*, Planar Laser Induced Fluorescence (PLIF) when pulsed laser systems are employed.

The LIF technique used in the present study involves only transitions between the ground X $^2\Pi$ and excited A $^2\Sigma^+$ states of nitric oxide (NO) which are shown in Fig. 1.3, corresponding to the NO γ bands. The related rates of stimulated absorption b_{12}, stimulated emission b_{21}, spontaneous emission of fluorescence A_{21}, and collisional quenching Q_{21}, are also labelled in this diagram. A more accurate description of this process is based on a multi-level fluorescence model which takes into consideration rotational energy transfer (RET) processes in both ground and excited states [5].

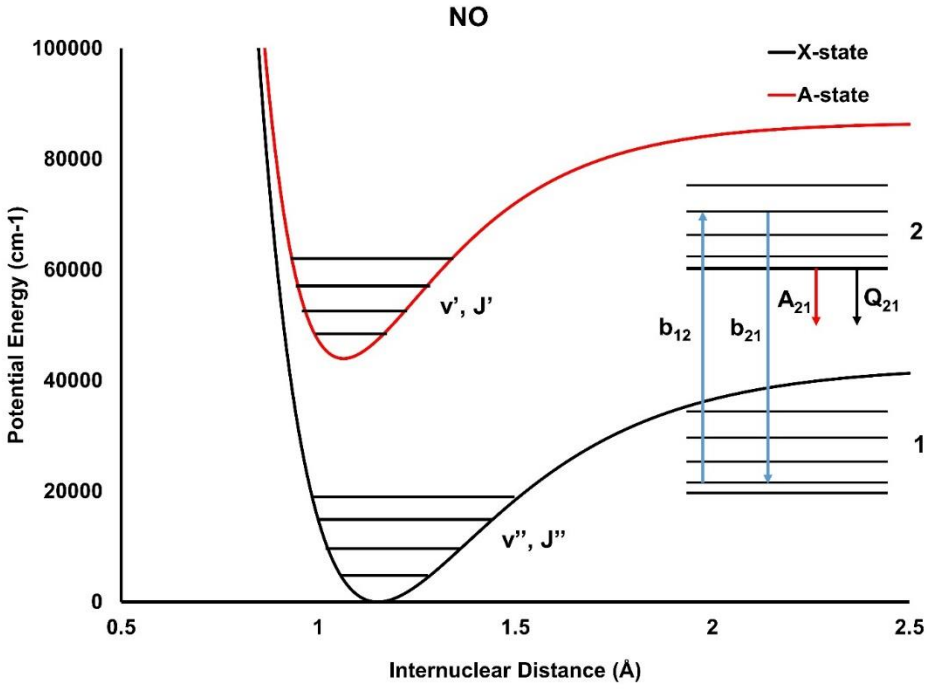

Fig. 1.3. Potential energy diagram of NO and two-level LIF model.

A concise description of NO spectroscopy can be found in the book by Herzberg [33] and only a brief overview closely related to the present study is presented here. Nitric oxide is an unusual diatomic molecule with an odd number of valence electrons. The electronic configuration in the ground state ($X\ ^2\Pi$) is $(\sigma)^2\ (\sigma^*)^2\ (\sigma)^2\ (\sigma^*)^2\ (\sigma)^2\ (\pi)^4\ (\pi^*)^1\ (\sigma^*)^0$. The unpaired electron occupies an antibonding π* orbital and this electron can be promoted to an upper *s*-type Rydberg nonbonding orbital, resulting in a shorter bond length of the excited $A\ ^2\Sigma^+$ state, as noted in Fig. 1.3. The interaction between electron orbit, electron spin, and nuclear rotation in the NO, causes a splitting of the degenerate electronic energy levels.

The interaction of electron orbit and spin in the ground state, $X\ ^2\Pi$, where $\Lambda > 0$, causes spin-orbit splitting, resulting in two states, $X\ ^2\Pi_{1/2}$ and $X\ ^2\Pi_{3/2}$. Different from the $X\ ^2\Pi$ state, the excited $A\ ^2\Sigma^+$ state where $\Lambda > 0$, does not show spin-orbit splitting. But the interaction between the electron spin and the nuclear rotation causes spin-nutation splitting. Based on the Hund's coupling cases, the electronic states can be classified. The ground state shows an intermediate behavior between Hund's case a and case b. If the

total angular momentum is low, the ground state behaves more like Hund's case a, which is employed in the transitions in this thesis. The excited state belongs to Hund's case b. For the ground state, the total electronic angular momentum, Ω, is half-integral and given by $\Omega = \Lambda + \Sigma$ where Λ and Σ are components of electron orbital and spin angular momenta along the internuclear axis. The total angular momentum, J, can be described by J = Ω, Ω + 1, Ω + 2…, with J ≥ Ω. In the $A\ ^2\Sigma^+$ state, the orbital angular momentum Λ and nuclear rotation N form a total angular momentum, K, which couples with electron spin to produce J given by J = (K + S), (K + S - 1), (K + S - 2)…(K - S).

According to the selection rules of ΔJ = 0, ±1, and of symmetry that only terms of different signs can combine, + ↔ -, only six transitions for each of the two sub-bands of NO A – X system can be allowed. Since the doublet splitting in the $A\ ^2\Sigma^+$ state is too small to be resolved, the branches that differ only in the excited doublet state overlap and the twelve possible branches are reduced to eight resolvable branches: P_{11}, $P_{21} + Q_{11}$, $Q_{21} + R_{11}$, R_{21}, P_{12}, $P_{22} + Q_{12}$, $Q_{22} + R_{12}$, and R_{22}. Fig. 1.4 shows a simulated excitation spectrum of each sub-band with each branch labeled in a different color. The studies in this thesis employ both the NO (0, 0) and NO (1, 1) bands. The spectrum of NO (1, 1) are very similar to that of NO (0, 0). The simulation spectrum for a mixture of 50% NO (v'' = 0) and NO (v'' = 1) at 300 K is presented in Fig. 1.5. The intensity difference between the two spectra is due to different Franck-Condon factors.

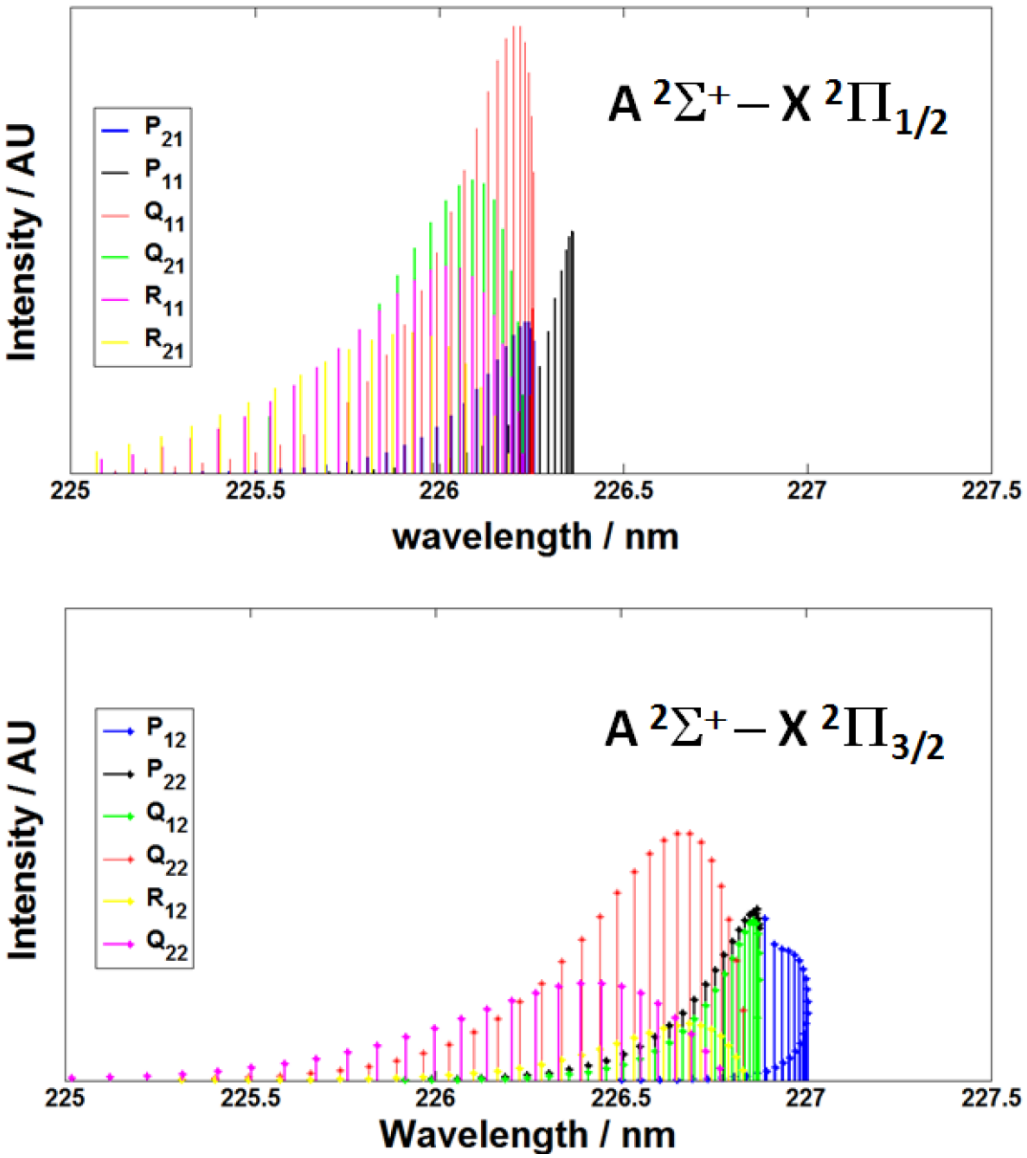

Fig. 1.4. Simulated nitric oxide excitation spectrum showing the 6 branches. The relative intensities reflect the ground state populations at 300 K [7].

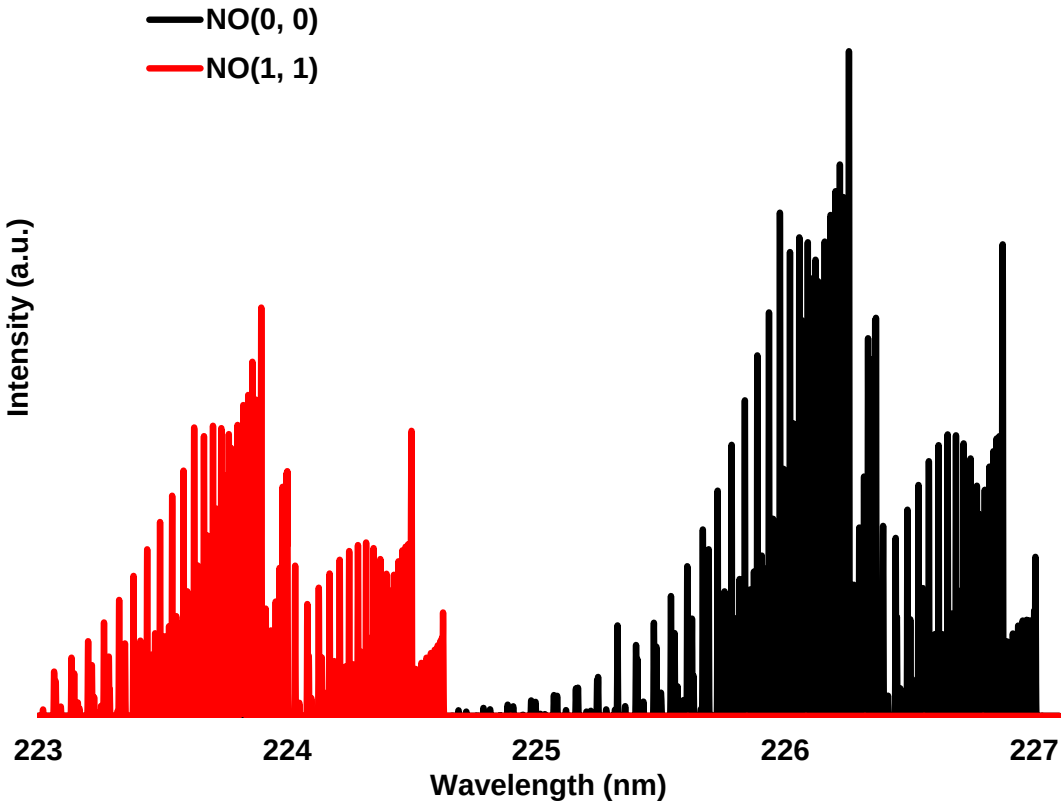

Fig. 1.5. Simulated NO (0, 0) and (1, 1) spectrum at 300 K [34, 35].

1.4.2 Two-line Thermometry

The collected fluorescence signal intensity, S_{LIF}, is a function of population in the excited state, N_2, emitted photon energy, the solid angle of collection $\Omega/4\pi$, and the collection volume imaged onto the detector V, as shown in Eq. 1.7.

$$S_{LIF} = A_{21} N_2 \frac{\Omega}{4\pi} h\upsilon c V \quad \text{(Eq. 1.7)}$$

The populations of the two states, N_1 and N_2, can be described by the rate equations:

$$\frac{dN_1}{dt} = -b_{12}N_1 + (b_{21} + A_{21} + Q_{21})N_2 \quad \text{(Eq. 1.8)}$$

$$\frac{dN_2}{dt} = b_{12}N_1 - (b_{21} + A_{21} + Q_{21})N_2 \quad \text{(Eq. 1.9)}$$

Where b_{12} and b_{21} are stimulated absorption and emission rates. They can be expressed by $b_{12} = B_{12}I_\upsilon\Gamma/c^2$ and $b_{21} = B_{21}I_\upsilon\Gamma/c^2$, where B_{12} and B_{21} are Einstein stimulated absorption and emission coefficients, respectively, with units of m^3/Js^2, I_υ is the spectral irradiance in W/cm^2cm^{-1}, Γ is the overlap function between the laser and absorption lines, and c is the speed of light.

Since the electronic excitation of NO requires a photon absorption in the UV, the population of the excited state is zero at the beginning of the laser pulse. Given that the total population is conserved and steady state is assumed, thus

$$N_1 + N_2 = N_1^0 \quad \text{(Eq. 1.10)}$$

Eq. 1.3 can be solved to produce:

$$b_{12}N_1 = (b_{21} + A_{21} + Q_{21})N_2 \quad \text{(Eq. 1.11)}$$

Combining Eq. 1.10 and Eq. 1.11 provides the population of the excited state.

$$N_2 = \frac{b_{12}N_1^0}{(b_{21}+b_{12}+A_{21}+Q_{21})} \quad \text{(Eq. 1.12)}$$

$$N_2 = N_1^0 \frac{B_{12}}{(B_{21}+B_{12})} \frac{1}{1+\frac{(A_{21}+Q_{21})\,c^2}{(B_{21}+B_{12})I_\upsilon\Gamma}} \quad \text{(Eq. 1.13)}$$

$$N_2 = N_1^0 \frac{B_{12}}{(B_{21}+B_{12})} \frac{1}{1+\frac{I_\upsilon^{sat}}{I_\upsilon}} \quad \text{(Eq. 1.14)}$$

Where $I_\upsilon^{sat} = \frac{(A_{21}+Q_{21})}{(B_{21}+B_{12})}\frac{c^2}{\Gamma}$

Finally, we obtain:

$$S_{LIF} = A_{21}N_1^0 \frac{B_{12}}{(B_{21}+B_{12})} \frac{1}{1+\frac{I_\upsilon^{sat}}{I_\upsilon}} \frac{\Omega}{4\pi} h\upsilon cV \quad \text{(Eq. 1.15)}$$

Since the full saturation is difficult to achieve in the present study where very high laser power are unavailable and the laser beam is formed into sheets, $I_\upsilon \ll I_\upsilon^{sat}$ and Eq. 1.15 results in:

$$S_{LIF} = N_1^0 B_{12} \frac{A_{21}}{(A_{21}+Q_{21})c} \Gamma I_\upsilon \frac{\Omega}{4\pi} h\upsilon V \quad \text{(Eq. 1.16)}$$

In this case, the fluorescence intensity depends on the laser intensity and quenching, and $\phi = \frac{A_{21}}{(A_{21}+Q_{21})}$ where expresses the fraction of molecules reaching the excited state that relax via fluorescence.

Due to the complexity of the NO spectrum, the development of a reliable laser-based diagnostic technique largely depends on a tunable excitation source with narrow linewidth capable of exciting single rotational transition. These types of lasers systems

have been commercially available for decades. By exciting a single rotational transition, the Boltzmann population of that specific state will be reflected on the fluorescence signal, therefore, the can be S_{LIF} written:

$$S_{LIF} = f_B N_1^0 B_{12} \frac{A_{21}}{(A_{21}+Q_{21})c} \Gamma I_\upsilon \frac{\Omega}{4\pi} h\upsilon V \quad \text{(Eq. 1.17)}$$

Where $f_B = e^{-E_{vib}/kT_{vib}}(2J'' + 1)e^{-E_{rot}/kT_{rot}}$

The Boltzmann population is a function of the vibrational and rotational energy of that specific state. The NO LIF two-line thermometry relies on the excitation of two different rotational states, J_1'' and J_2'', to obtain the fluorescence ratio R_{12} [31]. In this scheme, the two rotational states that are excited are within the same vibrational state (v'' = 0 or v'' = 1). The ratio R_{12} can be simplified as follows:

$$R_{12} = \frac{S_{f1}}{S_{f2}} = C_{12} \frac{(2J_1''+1)}{(2J_2''+1)} e^{-\Delta E_{rot}/kT_{rot}} \quad \text{(Eq. 1.18)}$$

Where the fluorescence collection efficiency, spectroscopic constants and laser intensity are combined and replaced by a constant C_{12}.

The C_{12} constant can be determined by measuring the fluorescence ratio with a known rotational temperature. The sensitivity of the two-line thermometry can be related to the percentage error of fluorescence ratio as well as the energy difference of the selected two rotational states and the determined temperature, as noted in Eq. 1.19.

$$\frac{\partial T}{T} = \frac{kT_{rot}}{\Delta E_{rot}} \frac{\partial R_{12}}{R_{12}} \quad \text{(Eq. 1.19)}$$

In order to increase the sensitivity of temperature determination, the energy difference of two rotational states should be as large as possible. However, a careful selection of two lines should be made to ensure that probing two rotational states can result in fluorescence images with acceptable signal-to-noise ratio. The temperature range studied in this thesis is 34 – 72 K. The Boltzmann populations at 34 K and 72 K are presented in Fig. 1.6.

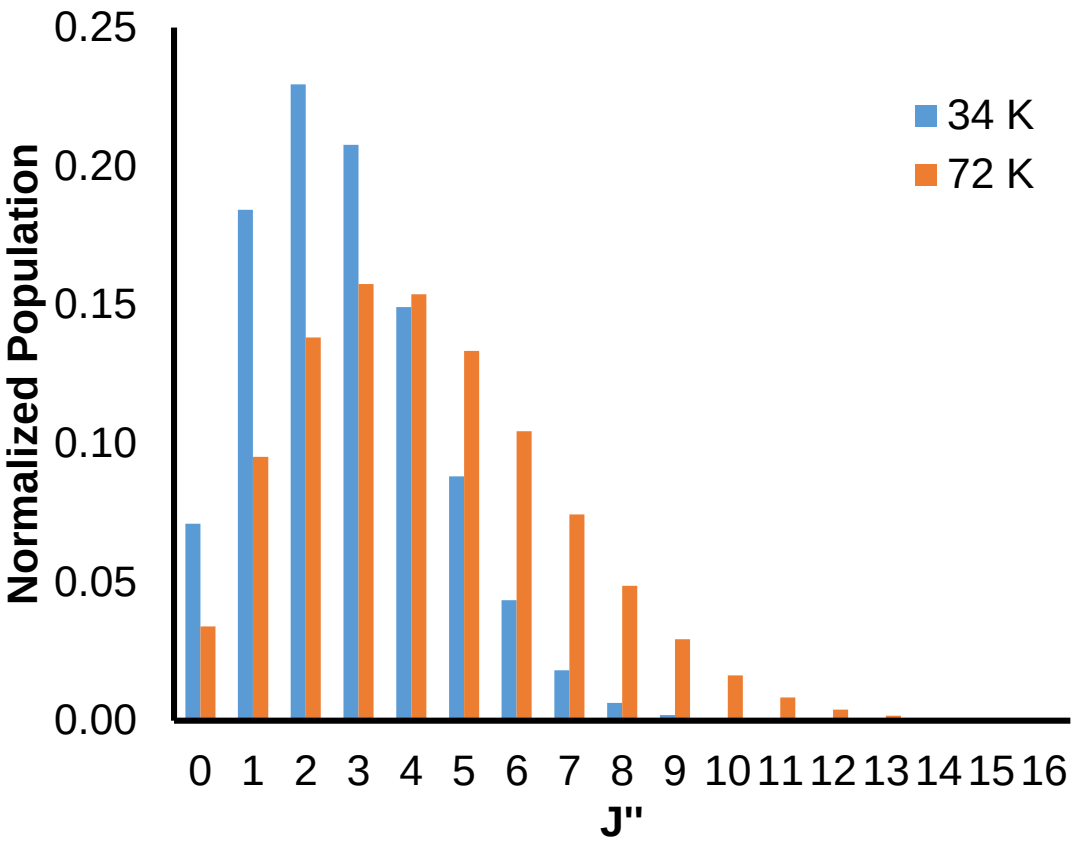

Fig. 1.6. NO Boltzmann normalized population at the lowest (34 K) and highest (72 K) temperatures for the flow fields studied in this thesis.

As shown in Eq. 1.18, the fluorescence ratio depends on the rotational temperature. But the pressure that affects the quenching levels in the studied flow can also affect the ratio, particularly when the two rotational levels in the excited state are involved. The excitations leading to different upper emitting rotational states are preferred due to the small separation between rotational levels of NO (B = 1.7 cm^{-1}) in order to achieve good temperature sensitivity. The excitation transitions in the present study are within the A ← X (1, 1) band, where no rotational level dependent collisional quenching has been observed [36]. In addition, our previous studies on temperature measurements relying on transitions within either NO A ← X (0, 0) or A ← X (1, 1) band have shown that quenching cross sections are not dependent on initial vibrational states [7].

1.5 Thesis Overview

This thesis is composed of four sections. The first section has provided an introduction to the motivation of the main research. The closely related studies and diagnostic techniques have been reviewed. Most importantly, the NO PLIF technique and related NO spectroscopy theoretical background have been addressed in this section.

The main research in this thesis has been conducted using a repetitively pulsed hypersonic flow test (rPHT) facility which was modified for stereoscopic imaging. An introduction to the facility will be briefly presented in the second section. More detailed description about the facility can be found elsewhere [4]. In the meantime, the wedge plate used to generate a shock wave and the position in the flow field will be described. The resulting flow properties in the post-shock region as a function of the wedge angle, such as velocity, pressure, and temperature, will be discussed and presented in detail. In addition, the VENOM technique utilized in the present study, that is, the NO_2 photolysis-based and recently developed invisible ink techniques, will be displayed along with their merits and drawbacks in this section. The images processing procedure will also be briefly described, but the focus will be a geometric reconstruction algorithm for the determination of three-dimensional displacements.

The measurement of three-component velocity and temperature will be demonstrated in the third section. This section consists of two main parts. The velocity measurement results obtained via NO_2 photodissociation VENOM will be firstly presented and compared to the prediction based on the flow conditions. Furthermore, the simultaneous measurement of velocity and temperature will be shown and possible reasons for the deviations from the predicted results will be discussed. Following the measurement with the NO_2 photolysis approach, the results of the simultaneous measurement via the invisible ink method will be presented. The NO seeding fraction effect on temperature determination will be discussed in this section.

The last section of this thesis will discuss the future work, particularly a comprehensive study of single-shot measurement of three-component velocity and temperature to obtain instantaneous fluctuations of the flow field. The feasibility of applying the stereoscopic VENOM to turbulent studies on high-enthalpy shock tunnels will be discussed in this section as well.

2. EXPERIMENTAL METHODS*

2.1 Laser Systems and Test Facility

In the previous VENOM scheme, a pulsed Spectra Physics PRO-230-10 Nd:YAG laser operated at 10 Hz produces a total power of 110 mJ/pulse at 355 nm [7]. The 9 mm diameter beam was expanded using a 2.5X beam expander and split with a 50:50 beam splitter into horizontal and vertical laser sheets to "write" a grid of NO (v'' = 0) and NO (v'' = 1) photoproduct from the NO_2 photodissociation. These orthogonal photolysis sheets can pass through a micro-cylindrical lens array or aluminum mesh to produce a modulation grid of NO photoproduct.

There are two identical PLIF laser systems that were used for the excitation of nitric oxide, each consisting of an injection-seeded Spectra Physics PRO-290-10 Nd:YAG laser operated at 10 Hz, with a linewidth of 0.003 cm^{-1}. The 532 nm output is used to pump a Sirah Cobra Stretch pulsed dye laser to produce a tunable fundamental output beam ranging from 600 to 630 nm using a solution of Rhodamine 610 and Rhodamine 640 in methanol. The fundamental output is mixed with the residual 355 nm from the Nd:YAG laser in a Sirah SFM-355 frequency mixing unit to produce up to 10 mJ/pulse at ~225 nm. The 225 nm beam was sent through a sheet forming optics and aligned to overlap the photolysis laser sheets.

Slightly different from the previous VENOM, in the recent VENOM scheme, one of the PLIF laser systems, used to "write" the grid, was tuned to excite the $R_1 + Q_{21}$ band head of the $A\ ^2\Sigma^+$ (υ' = 0) ← $X\ ^2\prod_{1/2}$(υ'' = 0) band near 226 nm, resulting in a grid of NO (v'' = 1) after spontaneous emission and collisional quenching from the A state. One or two PLIF laser systems were used to probe NO (v'' = 1).

All the dye laser systems were calibrated in the wavelength range of ~223 – 227 nm required for excitation of NO (0, 0) and NO (1, 1) bands right before the VENOM experiments. The calibration procedure has been clearly described in Sanchez-Gonzalez's thesis [7].

* Part of this section is reprinted with permission from "Stereo particle imaging velocimetry techniques" by Hui Hu, in Handbook of 3D Machine Vision, by Song Zhang, 2013, Taylor & Francis Group LLC Books, FL 33487 [24]. Copyright 2013 by Taylor & Francis Group LLC.

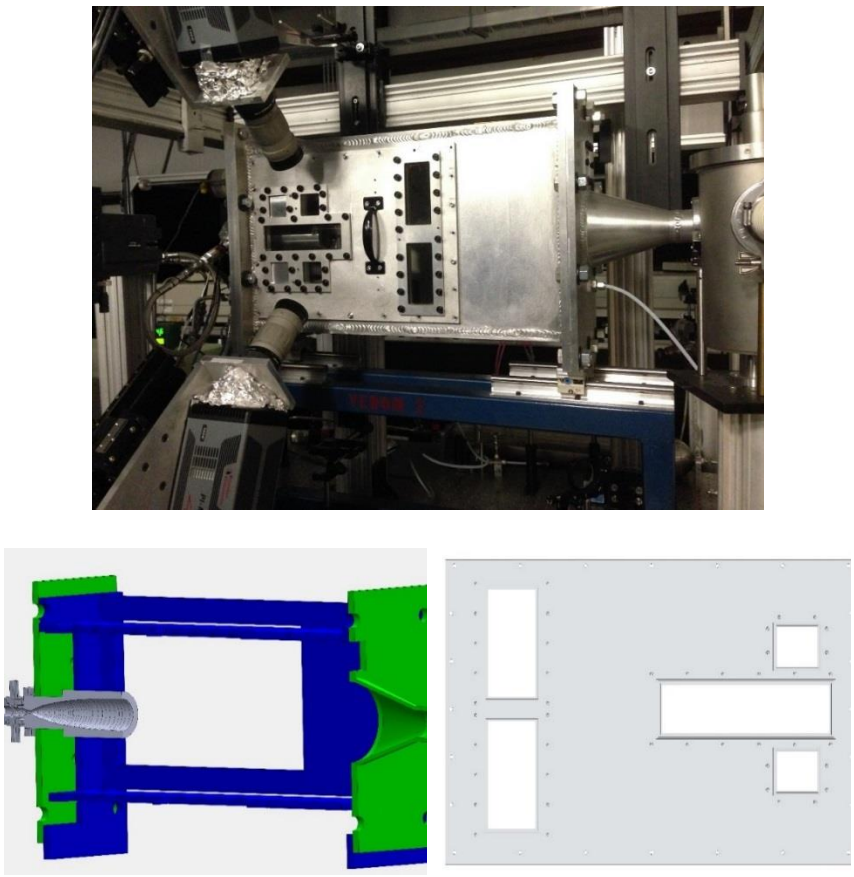

Fig. 2.1. Repetitively pulsed hypersonic test (rPHT) cell (top panel) fitted with a Mach 6.2 nozzle assembly (front cross-section view). The bottom right panel is a removable cell wall with recently modified square-size window.

As described above, the main research was carried out in the rPHT facility shown in Fig. 2.1. This apparatus was designed to enable advanced laser diagnostic development. The pulsed operation of the facility is synchronized to the laser pulses to achieve effectively continuous operation [4]. A major advantage of this model of operation is that the mass flow through the facility is reduced by several orders of magnitude as compared with a continuous flow facility. This repetitively pulsed flow test apparatus has been demonstrated with uniform supersonic flow at Mach 2.9, 3.8, 4.6 and 4.8 and hypersonic flow at Mach 6.2. The nozzle flows were characterized using fast-response pressure transducers and NO PLIF imaging for two-dimensional temperature and velocity measurements. The isentropic flow equations relating the ideal gas behavior to the nozzle

can be found in Sanchez-Gonzalez's thesis where the characterization procedure was also presented in detail [7]. In order to allow stereoscopic diagnostics development, the apparatus was modified to extend optical access via quartz windows, as seen on the bottom right panel of Fig. 2.1. The top and bottom slots on the front removable side wall were made to fit two quartz windows of 50.8 × 50.8 mm.

The nozzle assembly is composed of an aluminum feeding block fitted with three solenoid pulse valves and a screw-in aluminum axisymmetric converging-diverging nozzle. The gas is supplied radially to a settling chamber volume in the feeding block using three Parker General Valve Series 9 pulse valves controlled by a custom built valve driver circuit, which sends in externally 1.0-20.0 ms long pulses with ~250 μs opening times. In order to run the present Mach number (4.6 or 6.2) flow, each pulse valve was modified to have a 3 mm diameter exit orifice that was sealed with Viton gasket. Flow conductance calculations suggest that the settling time is on the order of 1.2 ms, consistent with time-resolved measurements, which show a comparable time to establish uniform flow at the nozzle exit.

The main chamber is evacuated using a pump assembly consisting of a Leybold E 250 rotary pump and a roots blower that provide a pumping speed of 70 L/s. The chamber pressure is continuously monitored using a calibrated pressure transducer (MKS series 902). Under static no-flow conditions, the pressure in the chamber is typically less than 0.2 torr. During operation, a needle valve connected to the chamber allows tuned pressure matching between the nozzle exit and the chamber.

2.2 Oblique Shock

As an object moves through a medium, molecules within the medium collide with each other and propagate information about the disturbance as a weak pressure wave which we perceive as a sound wave. This sound wave propagate at the speed of sound. If the object is traveling at a speed less than the speed of sound, the molecules are able to propagate information faster than the object's velocity. Thus, the fluid ahead of the object is "aware" of the object's incoming presence. Fig. 2.2 (a) shows the subsonic case [37]. However, if the object travels at a speed faster than the speed of sound, the molecules are unable to propagate information faster than the object's velocity. The sound waves that are emanated from the object start coalescing at the edges as seen in

Fig. 2.2 (b). This coalescence is called a shock wave and is at an angle μ to the object's velocity. Hence, shock waves are a compressible flow phenomenon when an object travels at or faster than the speed of sound.

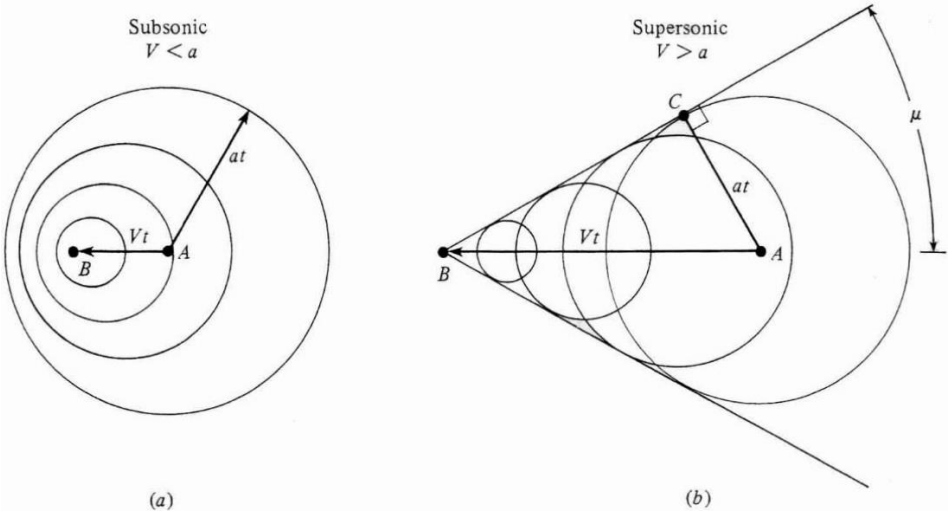

Fig. 2.2. Disturbances propagation by molecules in subsonic (a) and supersonic (b) flow [35].

In order to create an oblique shock wave, a wedge plate with a sharp knife leading edge was designed as seen in Fig. 2.3. The plate was mounted downstream from the nozzle exit vertically oriented and tilted some degrees with respect to vertical axial plane of the chamber. The nozzle flow interacts with the plate to generate an oblique shock wave shown in Fig. 2.4. The shock wave is in a plane titled with respect to the main flow direction. Even though the shock wave thickness is finite, the thickness is much smaller than any other length scale in the flow, so the shock wave is treated as a discontinuity in overall consideration.

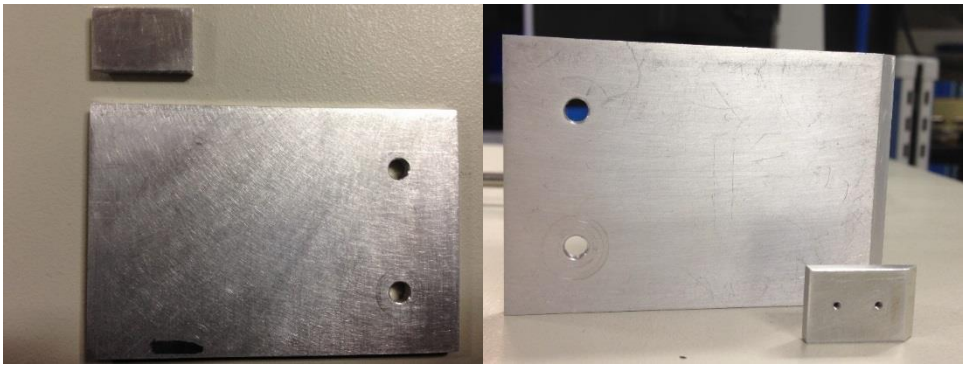

Fig. 2.3. Two types of wedge plates.

The fluid properties on either side of the shock wave are governed by the equations of conservation of mass, momentum, and energy. The flow properties after the shock are different from the flow field in the pre-shock area. The static temperature and pressure increase while the flow is deflected and speed decreases. The oblique shock flow field was chosen given the adjustability of the post-shock flow velocity, pressure and temperature conditions. The temperature, pressure, speed ratios are governed by the Mach number, wedge angle and gas heat capacity in the pre-shock flow field. More detailed description about oblique shock relations can be found in Anderson's book [37].

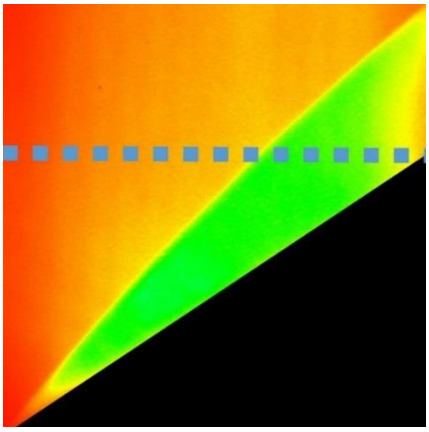

Fig. 2.4. NO PLIF image of an oblique shock wave (top view). The green area is the post-shock region.

The two types of wedge plates were tested within the Mach 4.6 and 6.2 nozzle flows. The large plate has a length, width, and thickness of 76.2 mm, 50.8 mm, and 3.1 mm, respectively and small one's length and width are 20.3 mm and 13.0 mm, respectively. The two nozzles have been previously characterized using rPHT facility and the exit flow profiles have been radially surveyed and compared with CFD results. The uniform, or inviscid, core region size is less than the actual nozzle exit diameter due to the boundary layer growth on the nozzle wall. The sizes in the Mach 4.6 and 6.2 flows were estimated to be approximately 15.9 mm and 33.0 mm, respectively [4]. When the large plate was mounted in the Mach 4.6 flow field, the post-shock region was limited by the core flow region which is no bigger than 15.9 mm. As noted in the dimensions of the large wedge, the width is larger than the core flow diameter. Even though the flow is pressure-matched, the shear layer can interact with the shock wave perturbing the post-shock flow field and thus reduce the region of stable post-shock area. In order to reduce the shear layer perturbation, the small one whose width is close to the Mach 4.6 core flow diameter was mounted instead, ensuring the entire plate is within the core flow area.

In the meantime, a new nozzle was designed to produce a steady flow with larger core flow region using the Method of Characteristics (MOC) [38]. The design was performed classically using the MOC with an ad-hoc Mach number increase to account for boundary layer displacement effects as estimated using simple integral methods assuming turbulent flow. A nozzle contour was generated from such calculations, which was employed to generate a Solidworks model and was built from an aluminum block using Computer Numerical Control (CNC) machining. The Solidworks model is shown in Fig. 2.5 which shows a larger exit diameter. The original target Mach number is 5.0. The nozzle inviscid shape was designed for uniform flow using the MOC. However, viscous boundary layers result in a reduced Mach number.

The nozzle was characterize via fast pressure measurements that was described elsewhere [7]. The miniature fast-response pressure sensors permitted measurements of the freestream pressure and Mach number. In the settling chamber upstream of the nozzle throat, Endevco-100 absolute piezoresistive pressure sensor was used, which has diaphragm-resonance frequency of 350 kHz and full-scale pressure of 100 psia. The sensing diaphragm is flush-mounted to the tip of the sensor and covered with a screen, leaving a small dead-air volume of under 0.005 cm^3, maximizing transient response. The

nozzle exit downstream was measured by a Kulite XCEL-100-5A transducer which was flush-mounted into the tip of a pitot tube. The transducer has a resonant frequency of 150 kHz and a 5 psia full-scale pressure.

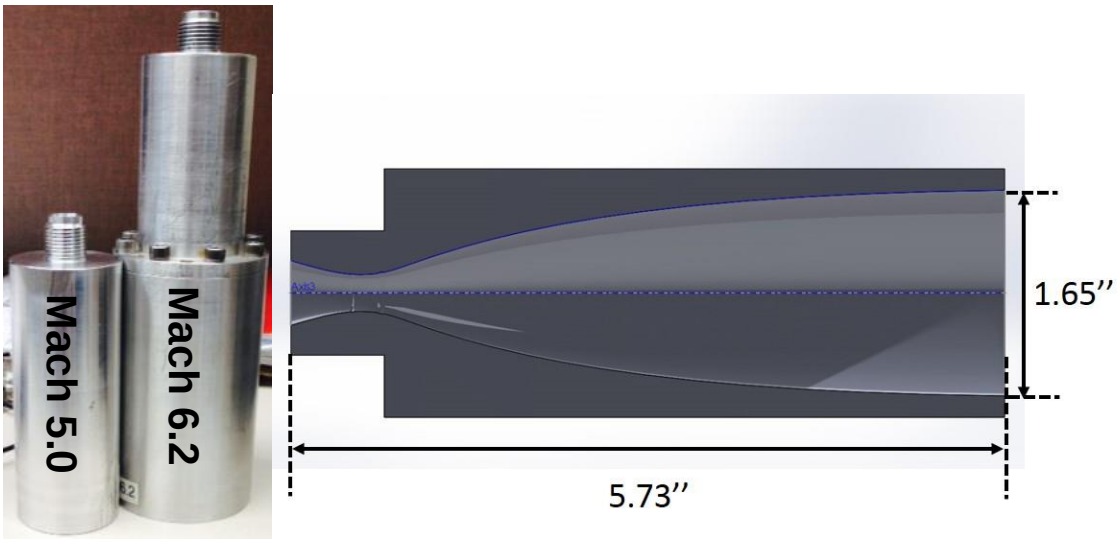

Fig. 2.5. Left panel is the designed nozzle in comparison to the Mach 6.2 nozzle. Right panel is the Solidworks model of the designed nozzle.

The pressure measurements showed that the settling chamber pressure fluctuated a lot, compared with the measurements on the Mach 4.6 and 6.2 nozzles. When the nozzle contour was examined, the settling chamber volume was smaller than those of Mach 4.6 and 6.2 nozzles. Since the downstream exit flow is correlated with the subsonic settling flow region, the fluctuation will be passed to the nozzle exit flow. Hence, the subsonic settling chamber volume should be expanded for smooth flow converging.

Given the fact that the designed nozzle was not appropriate for the experiments, the Mach 6.2 nozzle was instead installed into the rPHT cell for all the studies described in this thesis. Since this nozzle has been previously fully characterized, the exit flow conditions were used to derive the post-shock flow properties.

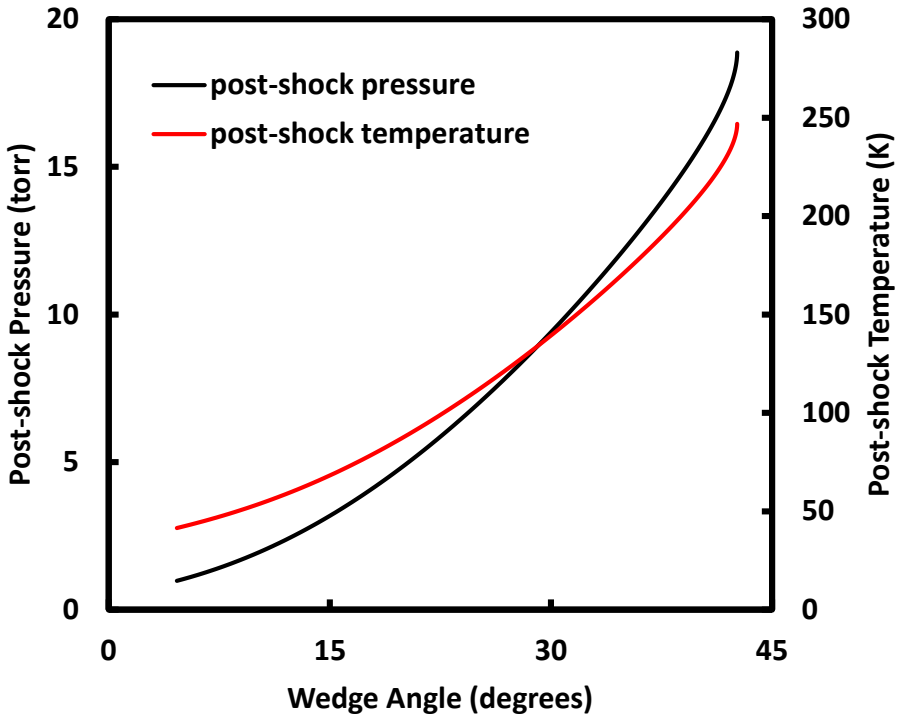

Fig. 2.6. The post-shock pressure and temperature variations versus the wedge angle given a pre-shock flow pressure of 0.5 torrr and temperature of 34 K.

The Mach 6.2 hypersonic flow is assumed in the pre-shock area and the temperature is calculated to be 34.0 ± 0.4 K known from nozzle characterization measurements. The post-shock temperature and pressure increase as a function of the wedge angle shown in Fig. 2.6. However, the total flow vector direction changes in the post-shock and total speed decreases. When the flow vector is decomposed in three dimensions, the streamwise component in the same direction to the pre-shock flow field decreases. Nevertheless, the out-of-plane component increases as the wedge angle becomes larger and then gradually decreases, as displayed in Fig. 2.7. Presumably the velocity is zero in the radial direction when the flow is pressure-matched and steady. As a result, the radial component will be zero in the post-shock as well. The tilted 16 degrees with respect to vertical axial plane of the chamber permitted significant out-of-plane motion of the flow past the shock wave. Given this wedge angle and velocity in the pre-shock region, the temperature and three-component velocity can be predicted based on

the oblique shock relations. However, this prediction is reasonable only in the core region of the Mach 6.2 flow field, the cylindrical volume with a diameter of ~33 mm. This issue will be further addressed in the following section.

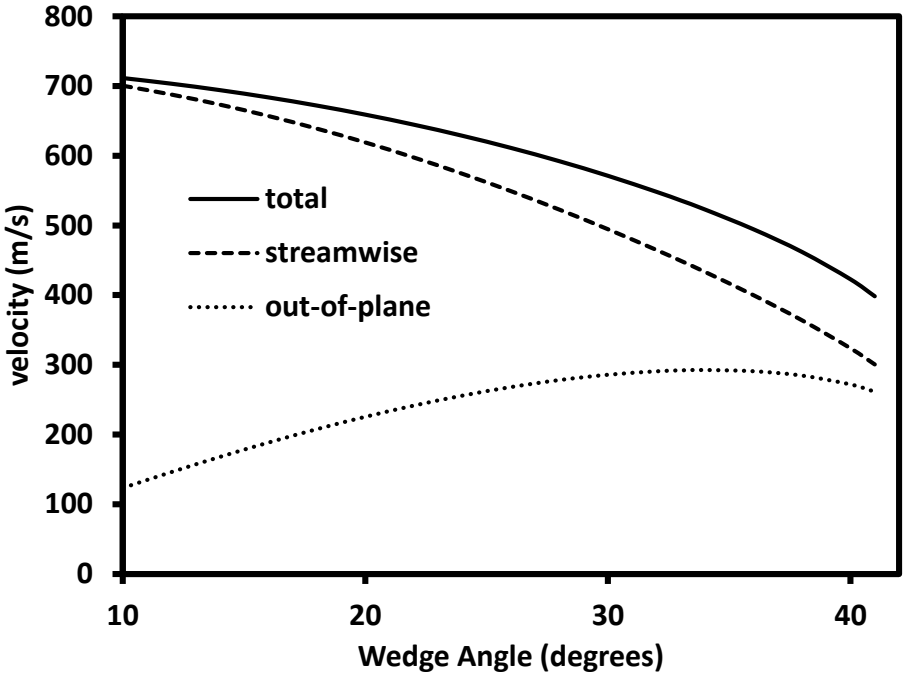

Fig. 2.7. The velocity in the post-shock area, including total speed and two components in the streamwise and out-of-plane directions, given the pre-shock velocity of 739 m/s.

2.3 Imaging System

A complete schematic of the laser systems and images acquisition set-up is shown in Figs. 2.8 and 2.9. The fluorescence images resulting from the excitation of nitric oxide were captured using two PI-MAX4 ICCD cameras (labeled as top and bottom cameras in Fig. 2.9) and fitted with a CERCO 100 mm *F*/2.8 UV lenses and extension rings. According to manufacturer specifications, this camera features a 1024 × 1024 imaging array and enables one to capture two images in rapid succession (separated by < 2 μs using a dual image feature (DIF)). In the meantime, it allows 16-bit digitization with up to 1 MHz to efficiently synchronize with high repetition rate lasers. This camera has a pixel width of 12.8 microns with a resolution limit of 39.1 line pairs per millimeter, or lp/mm.

however, the practical resolution of the optical system is reduced by a number of factors that include the quality of the lenses, the intensifier, and the fiber optic coupler [5]. The timing between the laser systems and cameras was controlled by a BNC 575 digital delay/pulse generator.

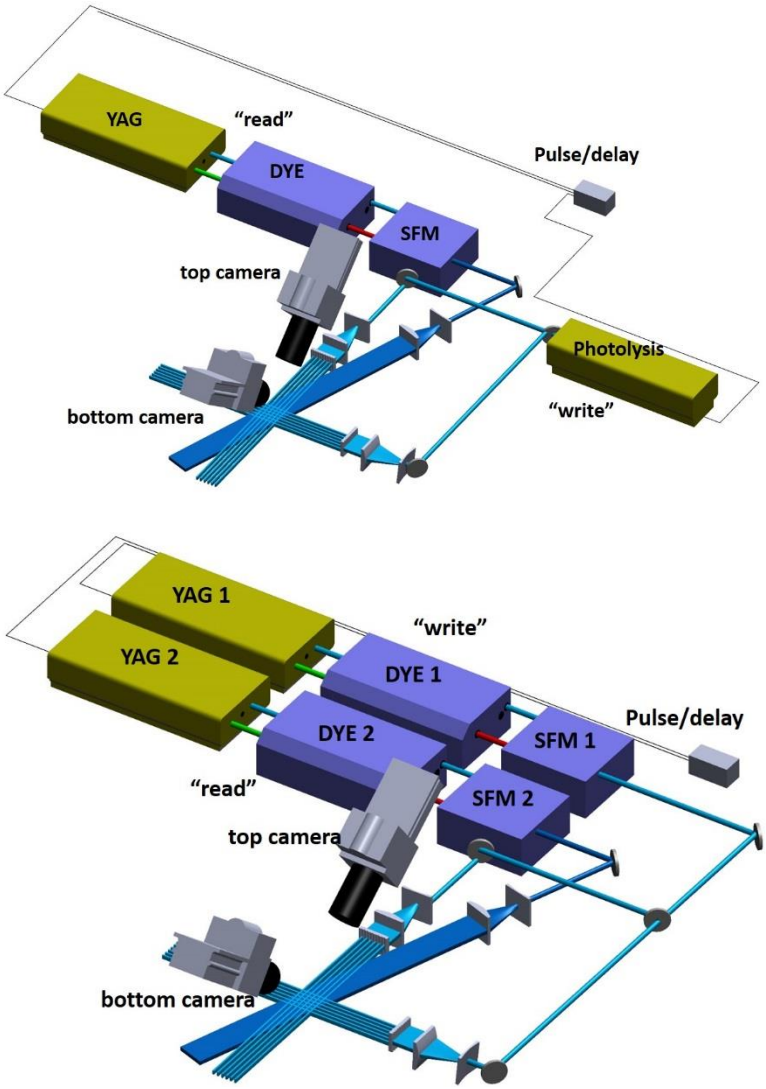

Fig. 2.8. Schematic of the two schemes of the laser diagnostic systems. NO_2 photolysis-based VENOM (upper panel) scheme and invisible ink (bottom panel) scheme.

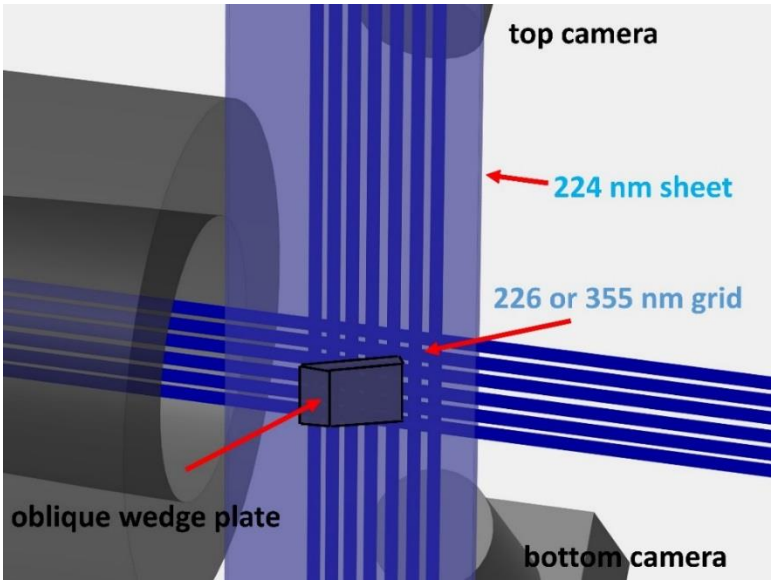

Fig. 2.9. Schematic of the experimental set-up and images acquisition setup [8].

2.3.1 Stereoscopic Image Recording

Three-component velocity determinations have been demonstrated using stereoscopic PIV [24]. The concepts and techniques can be applied to stereoscopic MTV. Three methods of stereoscopic image recording are summarized as follows:

(1) The lens translation method dictates that the two cameras used for stereoscopic imaging are mounted side by side with the image planes and the lens principal planes parallel to the measurement plane (the laser sheet), as shown in Fig. 2.10 (a). The ratio of the image distance to the object distance, or magnification factor, is constant across the entire acquired images. However, there are huge deviations when the magnification is variable due to the area-specific refractive index in the flow field, particularly liquid fluids. In the meantime the common area in the flow field viewed by both cameras is limited.

(2) Slightly different from the lens translation method, the general angle displacement arrangement requires that the image plane and lens plane are rotated with respect to the laser illuminating plane, as displayed in Fig. 2.10 (b). This method allows the two cameras to view much larger common area with better image quality than the lens translation method does. But there are

two main disadvantages. The plane with best focus is the one parallel to the image plane instead of the laser illuminating plane. It should be noted that the non-uniform focus related to finite depth of field using this method does not bring a major disadvantage to MTV applications. Secondly, smaller lens apertures (larger f number) are required to increase the depth of focus, which results in lower image intensity.

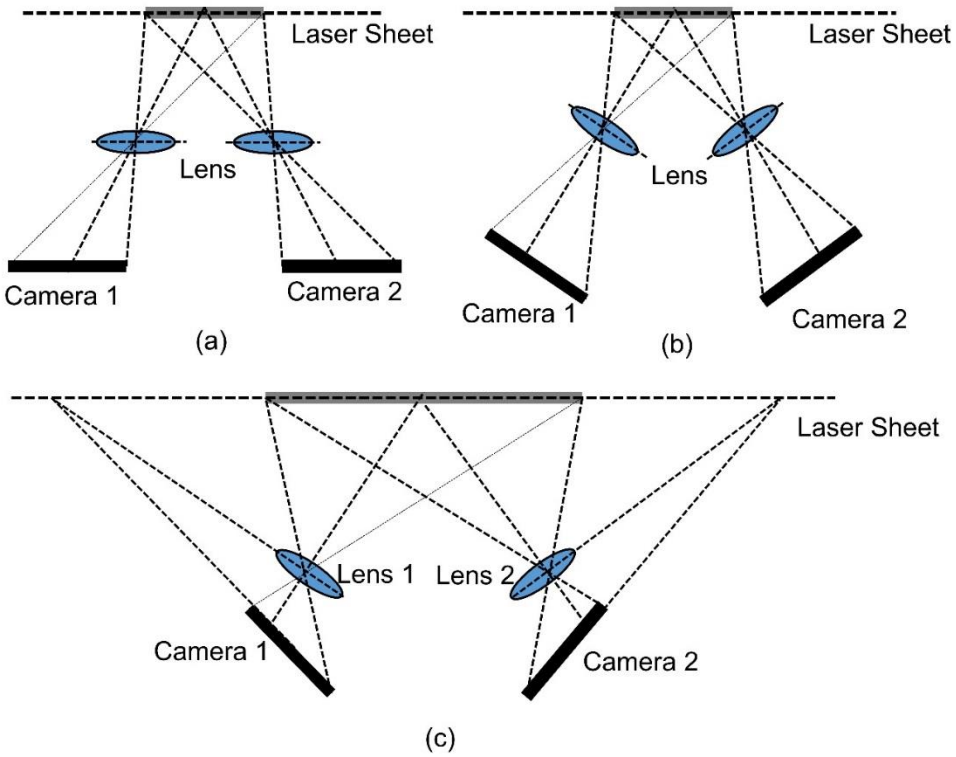

Fig. 2.10. Schematic of stereoscopic image recording methods. (a) Lens translation arrangement. (b) Angle displacement arrangement. (c) Angle displacement arrangement with Scheimpflug condition [22].

(3) As shown in Fig. 2.10 (c), the third method is similar to the general angle displacement method. Instead of making the image plane parallel to the lens plane, this plane and the lens plane intersect with the laser sheet plane at a common line to meet the Scheimpflug condition. Thus, the measurement

plane in the physical space can be focused onto the image plane of the cameras perfectly. This method overcomes the disadvantage of general angle displacement configuration and provide the best focus for the entire measurement window. It also enables the image sensors to be near the optical axis of the camera lenses so that the quality of the acquired images can be much better compared to the lens translation approach.

We have chosen the angle displacement method with the Scheimpflug condition for the VENOM experiments described in this thesis.

2.3.2 Geometric Reconstruction

The geometric reconstruction demonstrates how the three components of displacement vectors in the measurement plane in the physical space can be reconstructed from the two projected planar vectors in the image planes detected by the two cameras [23, 24]. Fig. 2.11 shows the schematic on how the three-dimensional displacements in the physical space are derived from the 2D displacement vectors. The origin is a known point within the measurement plane or laser illuminating sheet, which can be detected by the two cameras, with the physical coordinate of (x_0, y_0, z_0). Within a global coordinate system, x- and y-axes are aligned with the laser sheet, while the z-axis is normal to the laser sheet plane. The angles enclosed by the viewing ray and the light sheet normal direction are α_1 and α_2 for the respective viewing directions projected onto the x-z plane. Likewise, β_1 and β_2 are the angles within the y-z plane. In order to simplify the calculation, the two angles within the y-z plane are adjusted to be zero by tuning the position of the two cameras in the present study. Since the viewing distance is typically much larger than the displacement vector, the angle differences along the displacement vector are negligible. Thus, given the two projected planar vectors viewed by the two cameras and angles, the three components of displacement vectors in the physical space can be derived using the equations shown in Fig. 2.11.

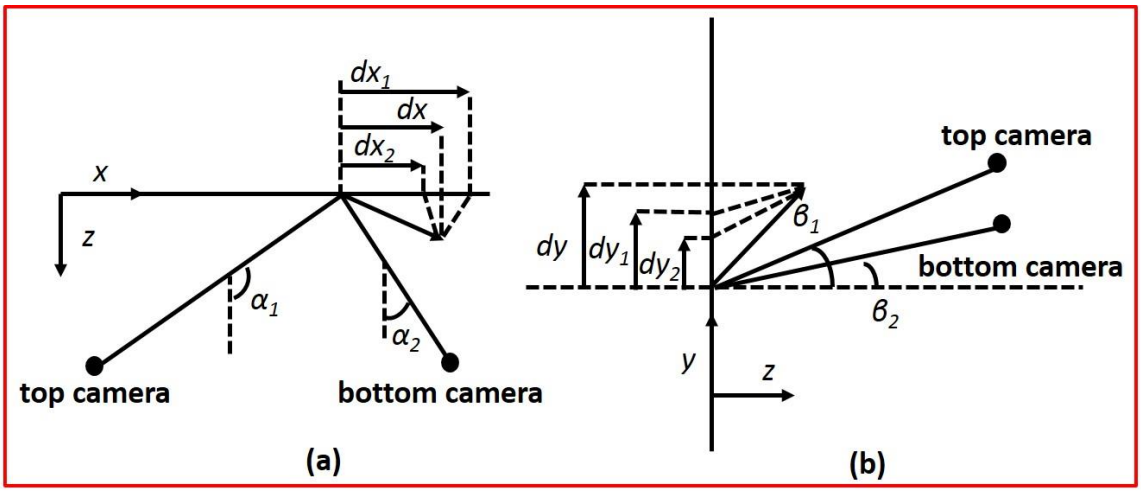

$$dx = \frac{dx_1 tan\alpha_2 - dx_2 tan\alpha_1}{tan\alpha_2 - tan\alpha_1}$$

$$dz = \frac{dx_1 - dx_2}{tan\alpha_2 - tan\alpha_1} = \frac{dy_1 - dy_2}{tan\beta_2 - tan\beta_1}$$

$$dy = \frac{dy_1 + dy_2}{2} + \frac{dz}{2}(tan\beta_1 + tan\beta_2) = \frac{dy_1 tan\beta_2 - dy_2 tan\beta_1}{tan\beta_2 - tan\beta_1}$$

Fig. 2.11. Geometrical description used for reconstruction of 3D-displacement field: (a) x-z plane; (b) y-z plane.

2.4 Images Processing Procedure

The images analysis procedure is described in this section on how to obtain three components of velocity and planar temperature. The analysis program was written in-house using Matlab, which includes several Matlab built-in functions. Several user-defined parameters were specified. In general, the estimation of two-dimensional displacement vectors is based on a procedure that tracks the displacement of fluorescence intersection patterns. Afterwards, the two-dimensional vectors were used to obtain the three components of velocity via the geometric reconstruction illustrated above. In addition, the generation of an intensity modulation pattern allows one to obtain flow temperature.

Since the planar temperature determination is similar to the 2D velocity and temperature measurement and the steps have been previously presented in Sanchez-Gonzalez's thesis [7], therefore the procedure is mainly focused on the determination of

three-component velocity. This procedure includes the steps of distortions and field-of-view correction, 2D cross-correlation, three-dimensional displacement vectors reconstruction and velocity determination. In order to illustrate this process, a dot-card glass on which numerous orthogonal lines were etched was mounted on an assembly of translational stages which can be operated in three dimensions. The intersections formed by the orthogonal lines can be readily used to track displacement vectors. In the meantime, the geometric reconstruction approach is verified by processing these images and the uncertainties of displacement vectors determination along the streamwise, radial, and out-of-plane directions were provided.

2.4.1 Pre-processing

The first step of the image analysis involves a pre-processing of all raw images that includes images averaging, smoothing, and the correction of distortions and field-of-view caused by the camera lenses. Although there are several common distortions, such as pincushion and barrel distortions and some variants of them, the main distortion in the present study is the field of view. The glass dot-card was imaged on the top and bottom cameras in a stereoscopic configuration with the Scheimpflug condition, as shown in Fig. 2.13. The enclosing angles of top and bottom cameras lenses were measured to be 40.9 and -38.1 degrees with respect to the normal direction of the imaging plane, respectively. In order to correct the field of view and distortions caused by lenses, an image was taken by a reference camera aligned normal to the imaging plane. This image was found to be slightly distorted mainly due to the imperfection of centering the camera via a single mounting arm, as shown in Fig. 2.12. This distortion is radially symmetric and affects mainly the area distant from the center of the image. In addition, the lines across the horizontal and vertical axes remain straight. An alignment angle was estimated used to rotate the image. The corrected image is shown on the right panel of the Fig. 2.12.

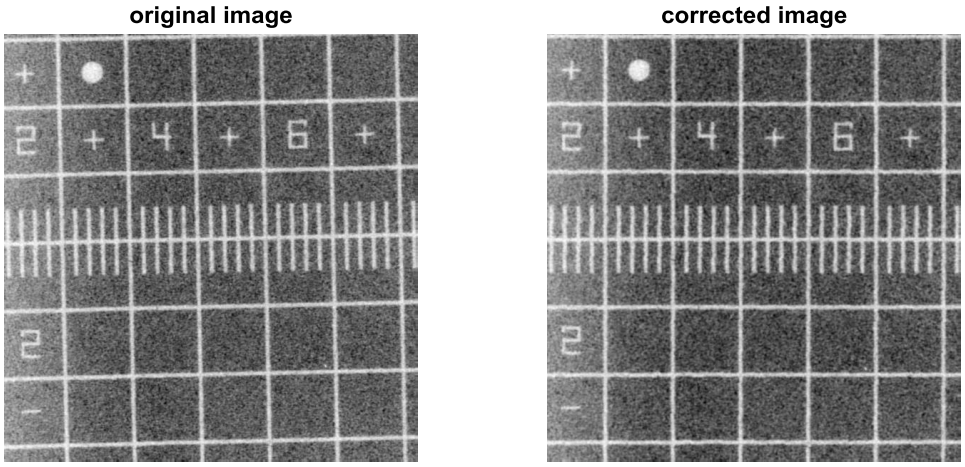

Fig. 2.12. Image alignment correction.

Due to the lenses of the top and bottom cameras in the stereoscopic configuration, the recorded images display different distortions and their field of view are different from the image recorded by the reference camera. An image registration was applied to the images, in which the images obtained by the top and bottom cameras were compared to the image recorded via the reference camera and aligned to the same field of view by a spatial transformation. This transformation requires mapping intersections on the images recorded via the top and bottom cameras to the equivalent pixel positions in the image taken by the reference camera. A number of grid intersections on the image acquired by the reference camera were chosen and their coordinates were recorded in a matrix. At the same time, the corresponding intersections on the images acquired via the top and bottom cameras were selected and the resulting matrixes were saved. Since there are several built-in position-locating functions in the image processing toolbox of Matlab, a program using these functions was written to locate those intersections precisely. A spatial transformation can be inferred using the coordinates of intersections, in which third or fourth order polynomial functions of the pixel positions, x and y, are automatically determined by Matlab and used for image mapping. After this image registration process, the image displays a homogeneous grid with straight lines in horizontal and vertical axes as seen in Fig. 2.14.

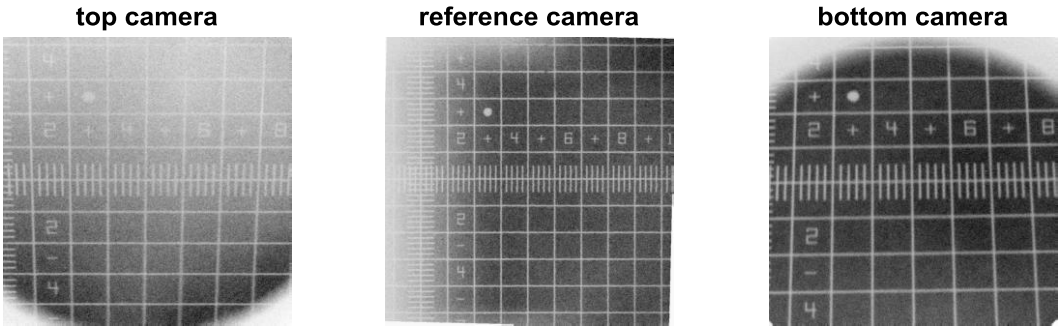

Fig. 2.13. Images obtained by the top and bottom cameras with the Scheimpflug condition.

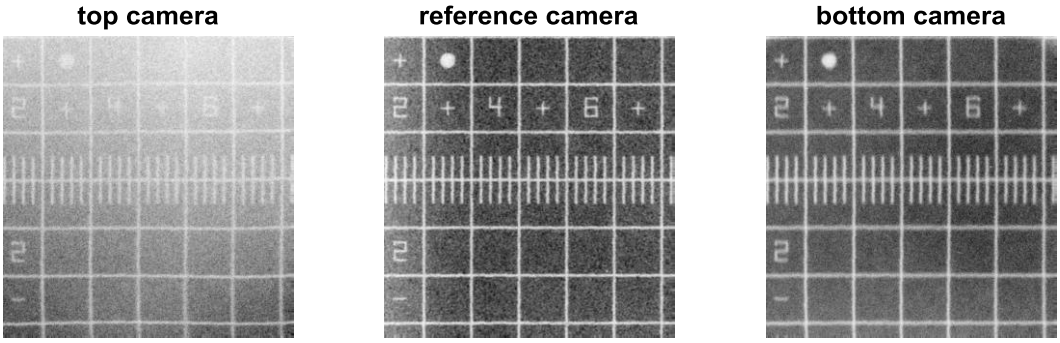

Fig. 2.14. Corrected dot-card images via image registration routine.

Since the images obtained by the top and bottom cameras were distorted in an entirely different way, the corresponding image registration routine was separately produced and applied to the rest of images obtained by each camera. Afterwards the images recorded via the top or bottom camera were ready to be processed via the cross-correlation procedure [7].

The corrected images from a specific camera were individually compared to the initial image shown in Fig. 2.14. Fig. 2.15 display the overlay of the initial and shifted images. The displacement vectors labelled with red arrows can tell in which direction and how much the dot-card was shifted. In order to help examine how the top and bottom cameras images infer the shift in the physical space, the streamwise direction is assumed to be from right to left and radial direction from bottom to top, as indicated by the white arrows in Fig. 2.15. It is noted that both cameras can image radial and streamwise shifts

in the exactly same directions in which the dot-card is moving, when a global coordinate system is assumed. The streamwise component of the red arrows from both cameras indicate the dot-card was shifted from right to left. Simultaneously, the arrows also show the card moved upward yet with different amount. The upward shifting is a combinative effect of radial and out-of-plane shifting of the dot-card. When the dot-card is shifting in the out-of-plane direction, the top and bottom cameras will record the shift in opposite directions. Since the upward shift recorded by the top camera is larger than that acquired via the bottom camera, the actual out-of-plane shift was regarded as an upward shift by the top camera, while it was treated as a downward shift by the bottom camera to compromise the amount of the radial component. Thus, it can be concluded that the dot-card was actually shifting away from the cameras in the physical space as indicated by the white solid circles in Fig. 2.15.

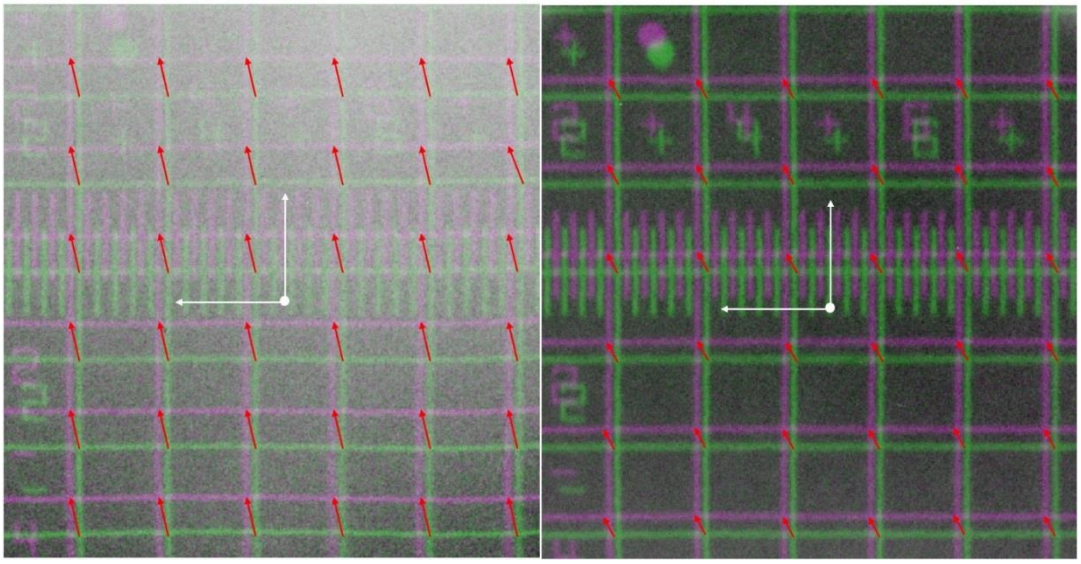

Fig. 2.15. The overlay of two images obtained by the top (left panel) and bottom (right panel) cameras.

2.4.2 Cross-correlation Analysis

The cross-correlation analysis is a spatial correlation technique used to estimate the displacement vector with high accuracy. Specifically, an interrogation area is defined

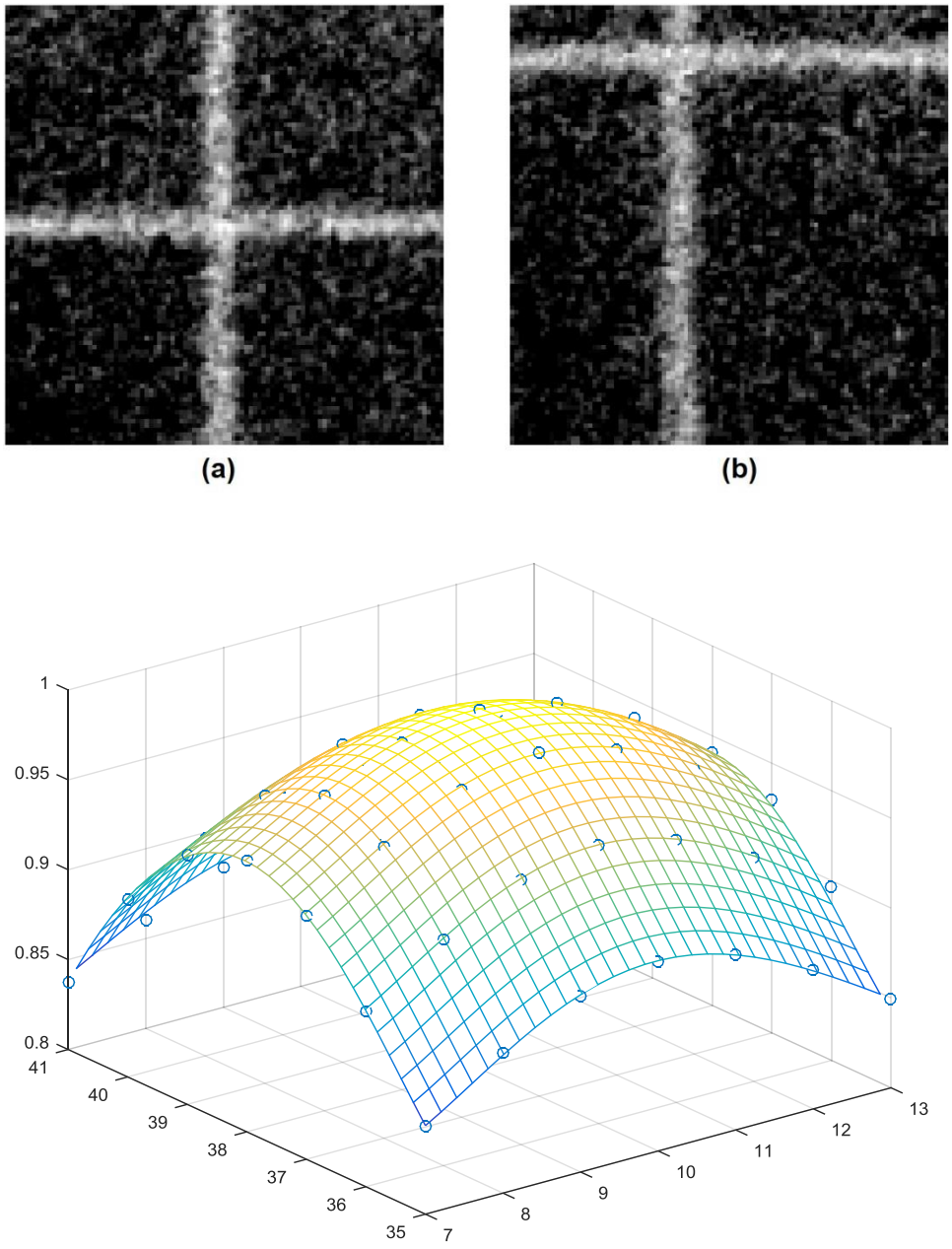

Fig. 2.16. Schematic of the cross-correlation analysis. Top panel shows the interrogated intersection of the initial (a) and displaced (b) image. Bottom panel presents the cross-correlation map to determine the displacement vector.

over each intersection and cross-correlated with its counterpart in the other image. The 2D cross-correlation technique permits a more accurate estimate of the difference in the location of each intersection between two images, since the comparison is not only dependent on the maxima or minima intensity of the intersections, but also on the entire intensity pattern that shapes the interrogated intersection. A cross-correlated map is generated in this cross-correlation routine. This map shows a maximum when the intensity pattern over the intersection is best aligned with its counterpart. The location of this maximum in the cross-correlation map indicates the displacement vector in the cross-correlated images. This process is illustrated in Fig. 2.16. The top panel in Fig. 2.16 shows the cross-correlated two images that include the interrogated intersections. The size of the two images is defined by the interrogation window dimension. The bottoms panel is the cross-correlation map in which the displacement vector was inferred from the maximum of the map.

The 2D cross-correlation represents an improvement to the simple maxima or minima tracking routine. Currently, the maxima tracking routine is used in the first step of cross-correlation procedure to find the location of intersections. When the maxima or minima are found, the interrogation windows are defined with appropriate dimensions to cross-correlate intensity patterns of the corresponding intersections. This technique is more advantageous than maxima or minima tracking routine for the analysis of single-shot fluorescence images featuring low signal-to noise ratio. A comparison of two techniques has been discussed in Sanchez-Gonzalez's thesis [7] on the analysis of synthetic single-shot images.

2.4.3 Displacement Vectors Reconstruction

Following the 2D cross-correlation analysis over the interrogated sections of images obtained by the top or bottom camera, both of 2D displacement vectors were used to obtain the three components of the displacement vectors via the geometric reconstruction described above. A number of tests were run to examine the sensitivity of each component to actual shifts and determination uncertainties in three dimensions. Table 2.1 displays the results of five of these tests. Each of these tests presents experimentally determined mean values along with 1σ root-mean-square (RMS) for the interrogated intersections and the actual shifts in three directions are provided in

parenthesis for comparison. The negative signs indicate that the directions in which the dot-card moved are opposite to the assumed global coordinate system.

Table 2.1. Experimentally determined mean displacements in three dimensions in comparison to actual dot-card shifts in parenthesis.

Item	**Streamwise** (mm)	**Radial** (mm)	**Out-of-plane** (mm)
1	-0.00±0.03 (0.00)	0.01±0.08 (0.00)	-0.83±0.09 (0.79)
2	0.57±0.04 (0.57)	-0.00±0.04 (0.00)	0.01±0.06 (0.00)
3	0.01±0.05 (0.00)	0.75±0.06 (0.76)	-0.00±0.08 (0.00)
4	-0.22±0.02 (-0.23)	0.77±0.08 (0.76)	-0.48±0.09 (-0.49)
5	0.28±0.03 (0.27)	0.75±0.05 (0.76)	0.33±0.07 (0.31)

The first three tests were run when the actual shifts occurred only in one dimension, i.e. out-of-plane (Item 1), streamwise (Item 2), radial (Item 3). The experimentally determined mean displacements were found to be comparable to the actual shifts within 5% deviation. This error is attributed to several factors that include the uncertainties within 2D cross-correlation routine and errors in angles measurement. As presented above, the reconstruction equations for determining the displacement vectors in radial and out-of-plane directions involve not only the 2D displacement vectors but also the angles (α_1 and α_2) enclosed by the viewing array and normal direction of the imaging plane, while the streamwise displacement vector is slightly affected by these angles. As a result, the streamwise uncertainty is much smaller than those in radial and out-of-plane directions. Since the out-of-plane displacement vector is extracted from the 2D radial vectors, two tests (Item 4 and 5) were run to investigate whether or not there is a bias in determining radial and out-of-plane displacement vectors from the 2D radial vectors. Table 2.1 shows that the results are consistent with those by shifting the dot-card in a single direction. Considering the small percentage errors in determining the three-

dimensional vectors, this geometric reconstruction is satisfactory in the implementation of 3D velocimetry.

2.4.4 Velocity Determination

As stated previously, molecular tagging velocimetry techniques are based on tracking tagged molecules as they displace through the flow field. The time-of-flight velocity is calculated by the distance moved by the tagged molecules divided by the time delay. The distance moved by the tagged molecules is calculated through the steps stated above. The measurement is a LaGrangian spatial average over the employed time delays, which is defined simply as,

$$u_{avg} = \frac{\Delta x}{\Delta t} \qquad \text{(Eq. 2.1)}$$

Where Δx is the spatial displacement from the images and Δt is the employed temporal delay.

The magnitude of the molecular displacement determines the spatial resolution of the velocity field. When the temporal delay reaches close to zero, the measurement produces an instantaneous velocity. However, this instantaneous measurement will suffer from large uncertainty due to the inaccuracy in determining short time delays. The gate width of cameras were set to be 30-100 ns depending on the fluorescence signal and laser pulse duration is ~10 ns. If the laser pulse duration and gate width are not negligible compared to the employed time delay within which the displacement occurs, this will result in an increased velocity uncertainty though there is an increase of the spatial resolution of the velocity measurements. This issue has been addressed by Danehy in boundary-layer and blunt fin measurements by taking into consideration gate width and laser pulse duration for the short time delay [39]. Thus, an appropriate time delay should be employed to make the measurement and gate width of cameras and laser pulse duration should be accounted for if necessary to improve the determination accuracy.

The fluctuations in pressure and temperature in the flow will affect nitric oxide quenching levels, thus affecting fluorescence lifetime and hence the effective time employed to calculate the velocity. Bathel et al. have investigated pressure and temperature effects on the velocimetry measurements when both images track one single fluorescence event [40]. An analysis was introduced to evaluate the weighted average of

each fluorescence profile as well as timing correction factor that are particularly relevant for long camera gates. However, the images were captured from two separate fluorescence events in the present VENOM experiments, such corrections are negligible and thus not applied.

The dominant random error in the velocity measurement comes from the signal-to-noise ratio of the fluorescence images. Since an accurate determination of the intersection location depends on the cleanliness of the intensity pattern, the signal-to-noise is defined in terms of the magnitude of the fluorescence modulation pattern rather than the overall fluorescence signal. This magnitude is determined by the size of “writing” lines as well as the quality of the optical system used to capture the images.

2.4.5 Thermometry

Given the fact that image pairs used for velocity analysis are recorded by both the top and bottom cameras, each camera can provide a planar temperature determination. The temperature analysis is based on fluorescence intensity as stated in the first section. When a specific rotational state is probed, a homogeneous temperature field should lead to uniform fluorescence images. However, the sheeting optics cannot possibly produce perfectly homogeneous probing sheet, resulting in inherent inhomogeneity. This effect is reflected on an inhomogeneous fluorescence image. A laser sheet intensity pattern is necessary for correcting the original image to produce an intensity-corrected image. Fig. 2.17 shows the contrast between corrected and uncorrected images. This pattern can be obtained by recording fluorescence images under static flow conditions or without the aluminum mesh. Running the imaging system at twice the pulsed valve repetition rate permits one to collect every other image without pulsed flow which can be regarded as the fluorescence image under static flow conditions. Another way to acquire the intensity pattern is to extract the intensity profile from the outer area of the flow field, which is proven to be efficient in single-shot instantaneous measurement. The acquired intensity pattern was normalized and used to correct the original image.

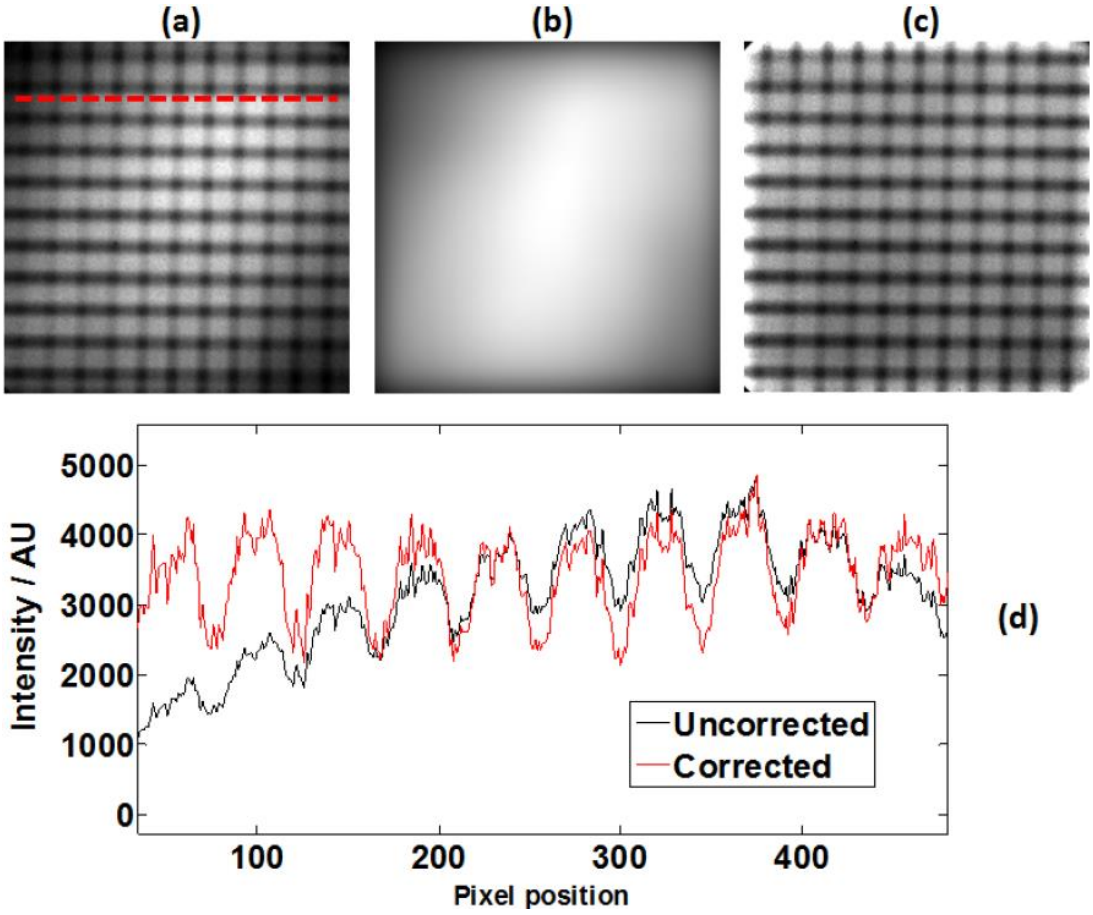

Fig. 2.17. Image correction for inhomogeneity in the probe lasers. Original image (a), correction image (b), corrected image (c). The fluorescence intensity profiles across the corrected and uncorrected images along a row are shown (d) [7].

As stated in the first section, the temperature across the flow field can be determined provided that the coefficient C_{12} is known. In the present experiments C_{12} was calculated by collecting images without pulsed flow, similar to the images collection for inhomogeneity correction. The coefficient was evaluated by averaging a large area within the camera field of view, with the same camera gain levels as those used to acquire the experimental images. As discussed in the first section, the collisional quenching of both $A\ ^2\Sigma^+$ (u' = 0) and $A\ ^2\Sigma^+$ (u' = 1) states is rotational-level independent. Thus, a determined single constant based on fluorescence ratio with a known temperature is sufficient to estimate the temperature of the entire flow field.

The 2D displacement vectors provide enough information to de-warp the second time-delayed fluorescence image resulting from the second probing event back onto the first time-delayed image acquired from the first probing event. Since the estimation of fluorescence ratios corresponding to the same flow elements can decrease the occurrence of grid artifacts in the temperature map. A second image spatial transformation was applied to the two time-delayed fluorescence images based on the velocity measurement. A consequence of the image de-warping is that the temperature measurement is averaged over the local displacements of the flow field within the employed time delay. Thus, the spatial resolutions of temperature and velocity measurements are determined by the magnitude of the molecular displacement.

3. STEREOSCOPIC VENOM MEASUREMENTS*

3.1 Measurement Principle

As stated above, the VENOM system provides combined planar MTV and two-line thermometry measurements using NO PLIF. The prototype VENOM technique using NO_2 photodissociation has been described elsewhere [7]. This section presents the measurement of three-component velocity and planar temperature using two different VENOM techniques which differ by means of producing vibrationally excited NO (v'' = 1) [6-9, 29]. After the flow was tagged with a "write" laser (a photolysis laser or PLIF laser system), one or two "read" laser systems were tuned to sequentially probe the A $^2\Sigma^+$(u' = 1) ← X $^2\prod_{1/2}$(u" = 1) band, with two time delays after the "write" laser. Following each probing event, the fluorescence was captured by the PI-MAX4 ICCD cameras in the stereoscopic configuration. This timing schematic is illustrated in Fig. 3.1.

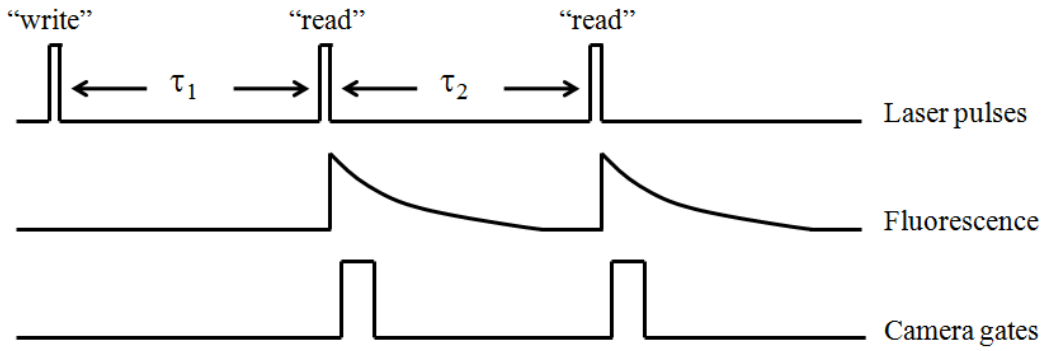

Fig. 3.1. Schematic of experimental sequence [5].

3.1.1 NO_2 Photodissociation Scheme

In this scheme, a trace amount of NO_2 is seeded into the flow of interest. A pulsed Spectra Physics PRO-230-10 Nd:YAG laser is used to photodissociate the NO_2 as follows:

$$NO_2 + hv_{355nm} \rightarrow \quad NO_{v=0} + O(^3P) \quad \sim 62\%$$

* Part of this section is reprinted with permission from "Simultaneous three-dimensional velocimetry and thermometry in gaseous flows using the stereoscopic vibrationally excited nitric oxide monitoring technique" by F. Pan, R. Sánchez-González, M. H. McIlvoy, R. D. W. Bowersox, and S. W. North, 2016 *Optics Letters*, 41, 1376-1379 [10]. Copyright 2016 by the Optical Society.

$\rightarrow$ $NO_{v=1}$ + O (^3P) ~38% Eq. (3.1)

The photolysis laser energy exceeds the dissociation energy of NO_2 in this process of Eq. 3.1. Hence, the process produces NO in two vibrational states (v'' = 0 and 1), with additional excess energy that is manifest in translation and rotation [41]. To perform velocimetry, the 355 nm photolysis beam was expanded with a beam expander using a 2.5X beam expander and split with a 50:50 beam splitter into horizontal and vertical laser sheets aligned through the area across the shock wave. The orthogonal photolysis sheets were passed through a micro-cylindrical lens array [42, 43] or an aluminum mesh [8, 9] to produce a modulation grid of NO photoproduct. Afterwards a 224 nm beam produced by the PLIF laser system was sent through a sheet forming optics and aligned to overlap the photodissociation laser sheets. The "read" laser was tuned to sequentially probe the A $^2\Sigma^+$(υ' = 1) ← X $^2\prod_{1/2}$(υ" = 1) band of NO with two time delays after the "write" laser, respectively. The time delays are chosen to allow for sufficient grid displacements for an accurate velocity determination and enough time for the thermalization process after photoexciation. The "read" laser sheet is thick enough in the area of interest during this time period to avoid possible biased out-of-plane motion tracking. The fluorescence images stemming from excitation by the "read" laser were captured using PI-MAX4 ICCD cameras and fitted with a CERCO 100 mm *F*/2.8 UV lens and extension rings, using a gate width of 50 ns. The cameras were aligned on the same side at 40.5 and –38.7 degrees with respect to the normal line of the laser sheets plane under the Scheimpflug condition. As a result, the measurement plane in the physical space can be entirely focused onto the detector plane of the camera.

3.1.2 Invisible Ink Scheme

As an alternative approach of NO (v'' =1) tagging, the vibrationally excited NO in the invisible ink scheme is produced by fluorescence and quenching from the NO $A^2\Sigma^+$ state [29]. This scheme is illustrated in Fig. 3.2.

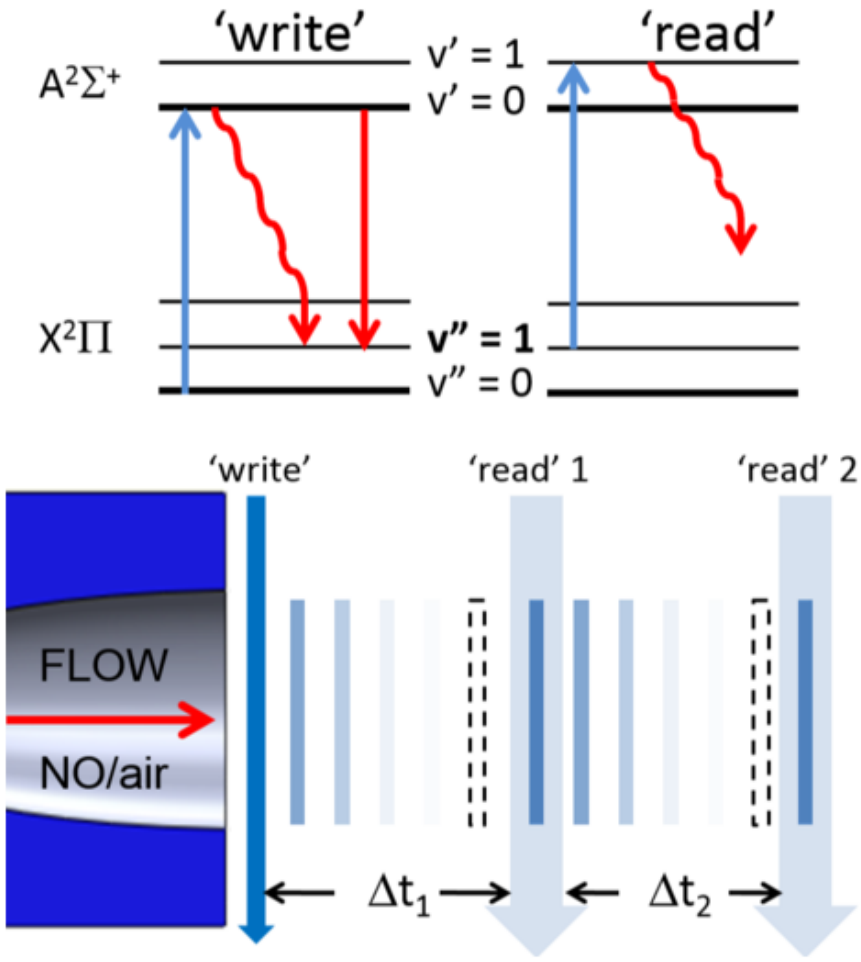

Fig. 3.2. Schematic of the invisible ink scheme as a variant of VENOM.

The gas mixture, consisting of a trace amount of NO in N_2, was flowed through the nozzle into the chamber to generate a pressure-matched and steady flow. The first laser system, used to "write" the MTV grid, was tuned to excite the $R_1 + Q_{21}$ band head of the A $^2\Sigma^+$ (u' = 0) ← X $^2\prod_{1/2}$(u" = 0) band near 226 nm, resulting in a grid of NO (u" = 1) after spontaneous emission and collisional quenching from the A state. The beam was also expanded with a beam expander and split with a 50:50 beam splitter, and sent through sheeting optics to "write" the grid of NO (u" = 1). The "read" process is entirely similar to that in the NO_2 photodissociation scheme. The vibrational distribution of NO (X $^2\Pi$) arising from A $^2\Sigma^+$ state fluorescence follows Franck-Condon dominated vibrational transition probabilities which favor low vibrational states, with 0.28 fractional yield at v'' =

1. Hancock at al. reported the nascent vibrational distribution of NO ($X\ ^2\Pi$) produced by both fluorescence and collisional self-quenching of NO ($A\ ^2\Sigma^+$, v' = 0) [44]. Several studies have investigated the reactive quenching of NO ($A\ ^2\Sigma^+$) [45, 46], leading to some cases in vibrational selectivity of the nascent distributions [46] or overall losses of the electronic ground state recovery due to NO reaction [45]. However, for the particular case of quenching by NO, reactive quenching is insignificant and thus the resulting quenching in the present study is approximately statistical [44]. The simulated vibrational distribution via fluorescence and collisional quenching is further discussed in the following section.

3.2 Velocity Measurements Using NO_2

A photolysis beam was expanded and split with a 50:50 beam splitter into horizontal and vertical laser sheets aligned through the area across the shock wave. The orthogonal photolysis sheets were passed through an array of ten 300 nm focal length, 2 mm wide micro-cylindrical lens based on the approach reported by Pitz and co-workers [42, 43]. This approach employing the lens array provides high laser intensity and narrow "written" regions via focusing. Hence, high NO photoproduct density and improved signal-to-noise levels can be achieved in this process. In addition, the narrow grid lines can simplify image processing and, in principle, result in more accurate determination of velocity. However, the narrow "write" lines limit the temperature determination to these bright lines.

The gas mixture of 3.5% NO_2/N_2 at the stagnation temperature of 294 K was flowed through the Mach 6.2 nozzle into the rPHT chamber maintained at 0.5 Torr to generate a pressure-matched and steady flow. The flow was pulsed at 0.5 Hz and the cameras acquisition was running at 0.5 Hz, to synchronize with 10 Hz pulsed laser systems via the pulse/delay generator. The flow interacted with the wedge plate centered 6 mm downstream from the nozzle exit, vertically oriented and tilted 15 degrees with respect to the vertical axial plane of the chamber. The "read" laser was tuned to sequentially probe the $A\ ^2\Sigma^+(\upsilon' = 1) \leftarrow X\ ^2\prod_{1/2}(\upsilon'' = 1)$ band head of NO with the time delays of 1000 ns and 2000 ns after the "write" laser, respectively. The fluorescence images were recorded by the top and bottom cameras with a gate width of 50 ns. The raw fluorescence images are shown in Fig. 3.3.

Additionally, just after excitation by the “write” laser, images of the fluorescence grid under static gas conditions were captured by the two cameras in stereoscopic configuration as well by a third reference camera aligned normal to the imaging plane. The positions of these grid intersections in the reference camera and their counterparts in the two cameras were used for field of view correction of all experimental images via image registration routines described in the second section.

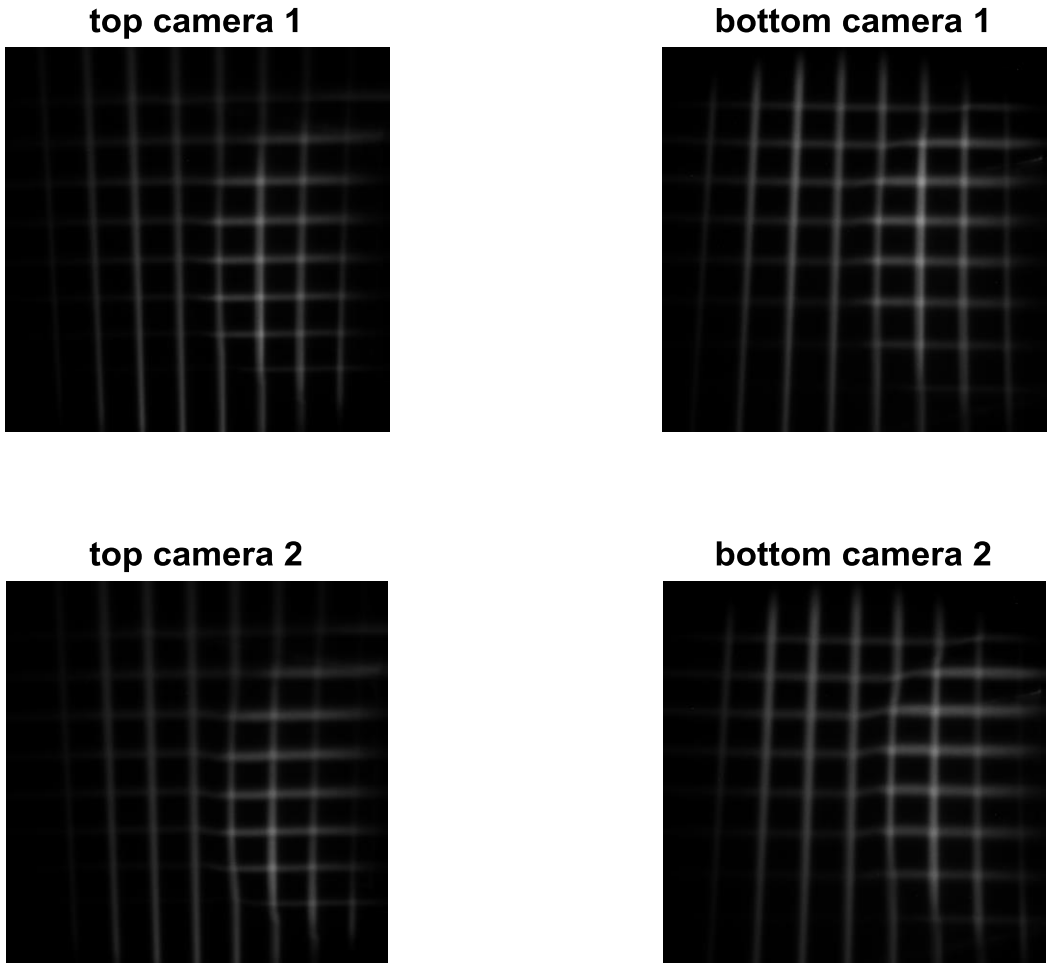

Fig. 3.3. Raw fluorescence images. They are acquired by the top and bottom cameras at the time delay of 1000 ns (top camera 1 and bottom camera 1) and 2000 ns (top camera 2 and bottom camera 2) using a micro-cylindrical lens array was used to “write” the grid of NO.

The corrected 100-shot average fluorescence images at the time delays of 1000 ns and 2000 ns showing the area of interest across the oblique shock are shown in Fig. 3.4. The flow is from the left to right and the images with a spatial resolution of 41.2 pixels/mm, display an area of 12.6×7.0 mm. The spatial resolution of the experiment was determined by acquiring images of the glass dot-card which was used for the geometric reconstruction representation with a grid formed by lines separated by 2.50 mm. The grid size was determined at different locations of the image. It was found that the spatial scale was homogeneous through the entire field of view. The overlay of the images at two time delays shows the grid displacement, as indicated by the red arrows. In the pre-shock area, the flow motion is seen as a shift of the grid intersections in each sequential images pair, where the displacements correspond to the streamwise and radial flow motion. In addition, the grid intersections in the post-shock area show a downward shift in the images acquired with the top camera (Fig. 3.4 (a)) and an upward shift in the images acquired with the bottom camera (Fig. 3.4 (b)). In principle, the grid deformations across the shock wave observed by the cameras in stereoscopic configuration result from the additive effect of radial and out-of-plane flow motion. Given the 2D nature of the test flow field, the radial component is negligible.

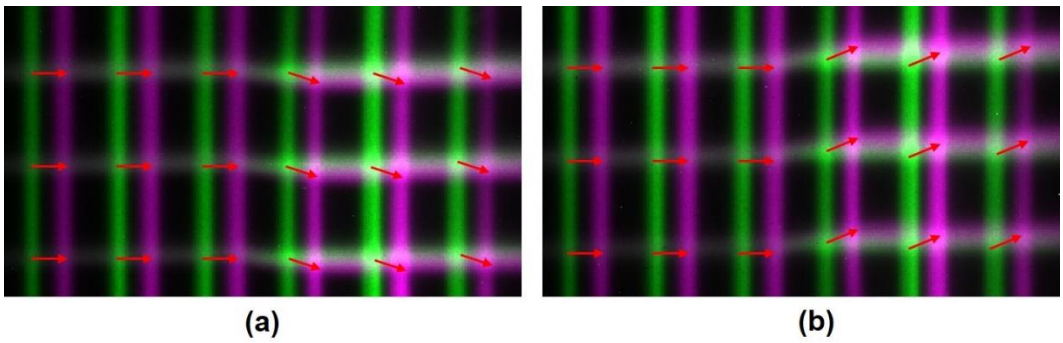

Fig. 3.4. The overlay of fluorescence images obtained by the top (a) and bottom (b) cameras. The read arrows indicate the displacement vectors.

The two field-of-view corrected time-delayed images acquired with each camera were employed to obtain local flow displacements at each grid intersection using 2D cross-correlation routines presented in Section 2.4.2. Then, three-component flow

displacements were determined *via* geometrical reconstruction based on the two-dimensional displacements. The resulting velocity component plots are shown in Fig. 3.5, where the streamwise velocity component in the pre-shock area resulted in 784 ± 2 m/s within 6% deviation from the predicted value of 739 m/s [4]. The post-shock streamwise velocity component decreases to 692 ± 23 m/s, which is consistent with the calculated value of 666 ± 9 m/s, based on a wedge deflection angle of 15 ± 1 degrees. The out-of-plane velocity measurement in the post-shock resulted in a value of 169 ± 22 m/s, within 5% deviation from the expected value of 178 ± 10 m/s. The out-of-plane velocity component before the shock wave is 23 m/s higher than the expected value of 0 m/s, while the radial velocity component is slightly below the predicted values of 0 m/s in both the pre-shock and post-region. The reported experimental uncertainties above correspond to spatial uncertainties (spatial root-mean-square deviations). Since there are limited number of the grid intersections in the pre-shock and post-shock area, the spatial uncertainties in both areas are quite large. As noted in Fig. 3.5, the streamwise velocity component is slightly curving up whereas the out-of-plane component is slightly curving down. When the interrogation area is much close to the right end of the wedge plate, the flow will surpass the edge, resulting in a decreasing out-of-plane component and increasing streamwise component. The slightly larger deviation of the out-of-plane component from the expected value could be attributed to several factors that include the poor overlap between the MTV grid and probe laser sheet as well as uncertainty in the wedge angle measurement leading to error in the assumed flow conditions.

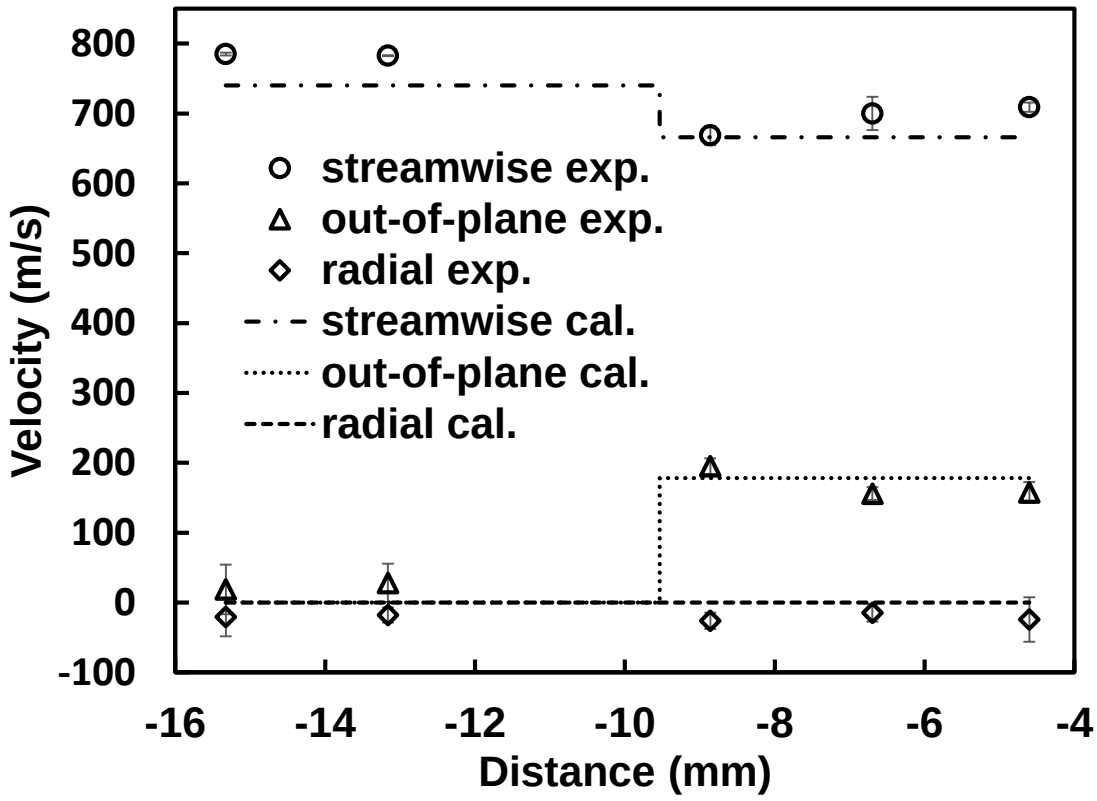

Fig. 3.5. Experimentally obtained streamwise, out-of-plane, and radial velocity components. The predicted velocity components are shown for comparison. The distance is measured with respect to the right end of the wedge plate (the origin of horizontal axes).

3.3 Simultaneous Measurement of Velocity and Temperature

In order to achieve the simultaneous measurement of three-component velocity and planar temperature, an aluminum mesh that generates bright regions of 0.84 mm width and dark regions of 0.25 mm width was employed in this measurement [8]. The 224 nm beam was sent through a sheet forming optics and aligned to overlap the photodissociation laser sheets. The "read" laser was tuned to sequentially probe the $A^2\Sigma^+_{1/2}$ (υ' = 1) ← $X^2\prod_{1/2}$(υ" = 1) band of NO on the $R_1 + Q_{21}$ (8.5) and $R_1 + Q_{21}$ (1.5) lines with time delays of 1.5 μs and 2.5 μs after the "write" laser, respectively. The fluorescence images stemming from excitation by the "read" laser were captured using the top and bottom cameras using a gate width of 50 ns. Similar to the images acquisition shown in

the previous section, images of the fluorescence grid under static gas conditions were captured at time zero after photodissociation with the two cameras as well as the third camera. The field-of-view corrected images are shown in Fig. 3.6.

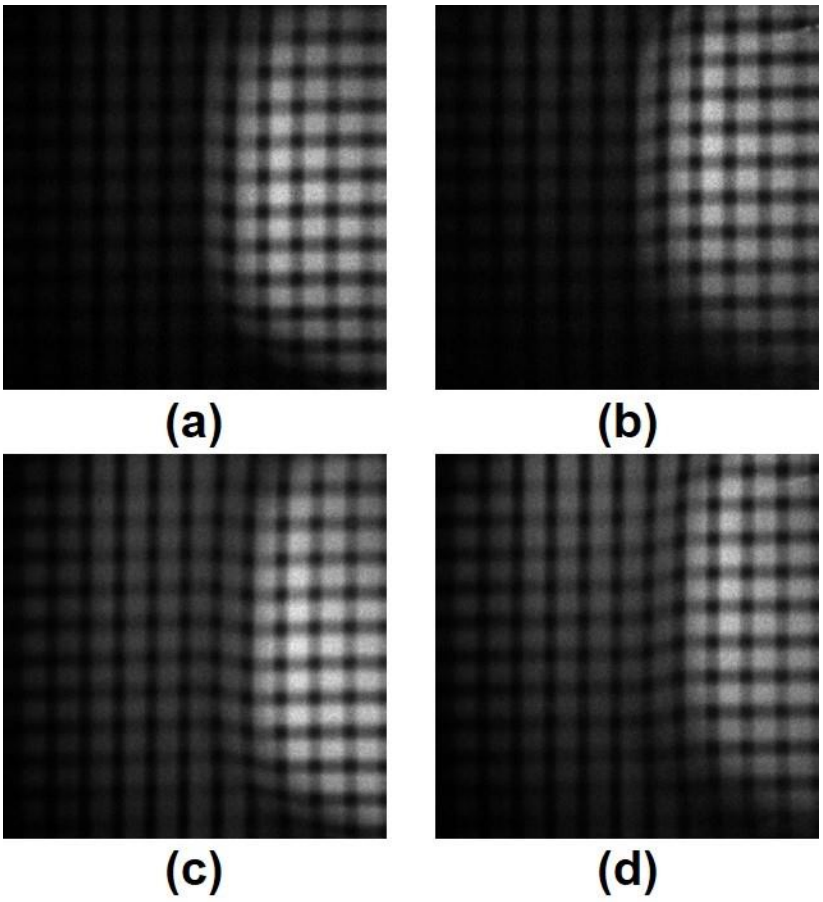

Fig. 3.6. Fluorescence J = 8.5 and J = 1.5 images taken by the top camera at the time delay of 1.5 μs (a) and 2.5 μs (c) using an aluminum mesh to “write” the grid of NO, respectively. Fluorescence J = 8.5 and J = 1.5 images taken by the bottom camera at the time delay of 1.5 μs (**b**) and 2.5 μs (**d**).

The flow is from left to right and 100-shot average images have a spatial resolution of 41 pixels/mm, displaying a field of view of 25×25 mm. The temperature effect on the Boltzmann populations and hence intensities of the probed states is clearly observed from

the comparison of fluorescence intensities in the pre-shock and post-shock flow field. At the time delay of 1.5 μs, the J = 8.5 image (Fig. 3.6(a) or (b)) taken by either top or bottom camera shows much higher fluorescence intensities in the post-shock flow than that in the pre-shock field, indicating the higher post-shock temperature. This effect is further corroborated by comparing the pre-shock signal of the J = 8.5 (Fig. 3.6(a)) and J = 1.5 (Fig. 3.6(c)) images taken by either top or bottom camera. This is attributed to an abrupt change of gas properties across the oblique shock wave, one of which is reflected on a sudden increase in the temperature field. Notably, despite the pronounced streamwise motion, the intersections of fluorescence minima spacing neighboring fluorescence grid from the top camera are horizontally misaligned at the shock approximately centered in the image and collectively moving down in the post-shock. In contrast, these intersections observed by the bottom camera are moving up. In principle, the grid deformations across the shock wave observed by the cameras in stereoscopic configuration result from the additive effect of radial and out-of-plane flow motion. Given the 2D nature of the test flow field, radial velocity should be negligible. Consequently, the area of interest was limited to the rectangular region near the center of the wedge where the flow conditions are well-defined.

In the case of the aluminum mesh approach previously reported by Hsu et al., tracking dark regions rather than the fluorescence maxima results in the same determination of the line displacements due to identical widths of bright and dark regions [5, 6]. Since a higher transmission aluminum mesh is used, tracking the dark intersections results in more accurate velocity than tracking the wider bright regions. Hence, the fluorescence images were pre-processed via intensity inversion before obtaining local flow displacements at each grid intersection using the 2D cross-correlation routine. The overlay of fluorescence minima images via intensity inversion are shown in Fig. 3.7.

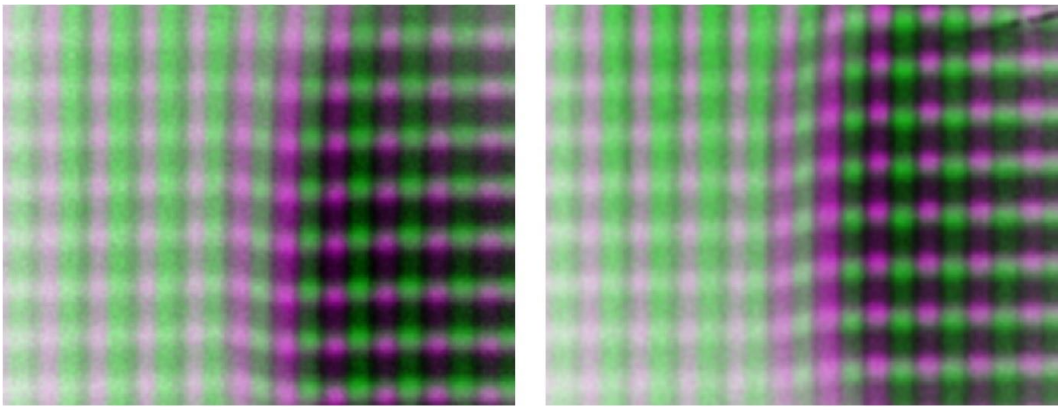

Fig. 3.7. Overlay of fluorescence minima images via intensity inversion (cropped) obtained by the top (a) and bottom (b) cameras.

Subsequently, three-component displacements in the physical space were calculated *via* geometrical reconstruction based on the two-dimensional displacements obtained with the top and bottom cameras. The velocity components in each of the interrogated intersections were interpolated using built-in functions in Matlab to produce the three velocity maps. The spatial filter size was carefully chosen to not exceed the optical resolution of the imaging system so that relevant flow field features are not arbitrarily smoothed. According to the velocity maps shown in Fig. 3.8, the streamwise velocity component in the pre-shock flow field gives a mean value of 785 ± 5 m/s within 6.2% deviation from the predicted value of 739 m/s, which is comparable to the streamwise motion determination using the micro-cylindrical lens array to “write” the fluorescence grid. Past the shock wave, the streamwise velocity component decreases to a value of 685 ± 7 m/s, which is consistent with the calculated values (666 ± 9 m/s) based on a deflection angle of 15 ± 1 degrees. The out-of-plane velocity measurement in the post-shock flow field resulted in a value of 193 ± 6 m/s, within 8.4% deviation from the expected value of 178 ± 10 m/s. The observed variance from zero of the out-of-plane velocity before the shock wave is mainly attributed effects of low signal-to-noise levels in this region when probing the J = 8.5 state.

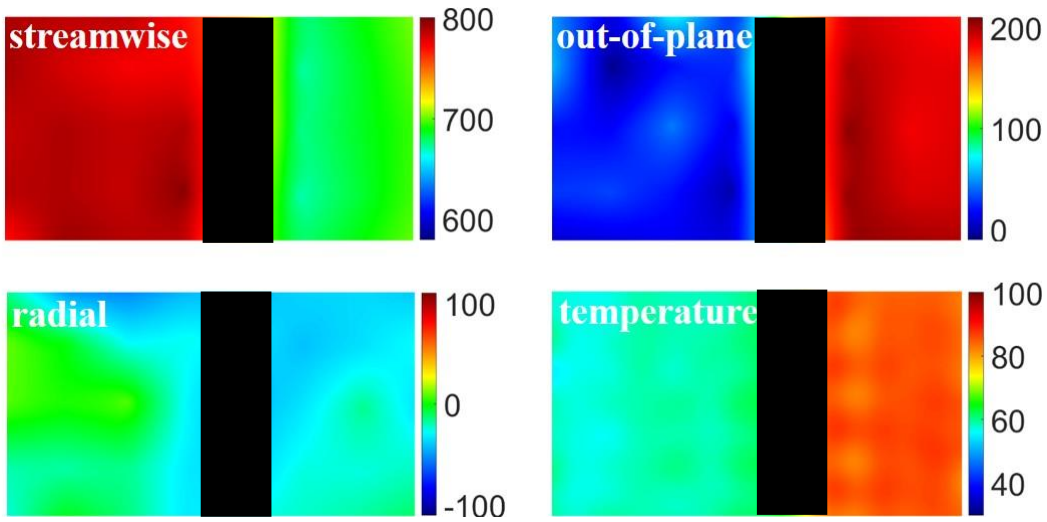

Fig. 3.8. Experimentally obtained streamwise, out-of-plane, radial velocity components (m/s) in the Mach 6.2 flow field across the oblique shock wave. Experimentally determined temperature (K) map using two-line thermometry.

The utilization of the aluminum mesh for tagging purposes leads to a modulation pattern of NO_2 photodissociation, permitting the determination of temperature field. The velocity measurement provides enough displacement information to de-warp the second time-delayed image onto the first one, allowing calculation of fluorescence ratios that correspond to the same flow elements [7-9, 29]. Temperature measurements using the VENOM technique are based on two-line thermometry and thus require a thermalized rotational distribution of the NO (X $^2\prod_{1/2}$, υ" = 1) photoproduct to indicate the true local flow temperature. Two independent temperature measurements were obtained by analysis of the image pairs acquired using the top and bottom cameras, as shown in Fig. 3.9 (a) and (b). We observed no strong dependence of the measured temperature on the position of the cameras. Also, the control experiment for the temperature measurement with reversed probing sequence (J = 1.5 image at 1200 ns and J = 8.5 image at 1800 ns) showed consistent results, suggesting the laser sheet thickness is a negligible factor. Fig. 3.9 displays the average temperature map in the area of interest from the two time-delayed images of the top and bottom cameras.

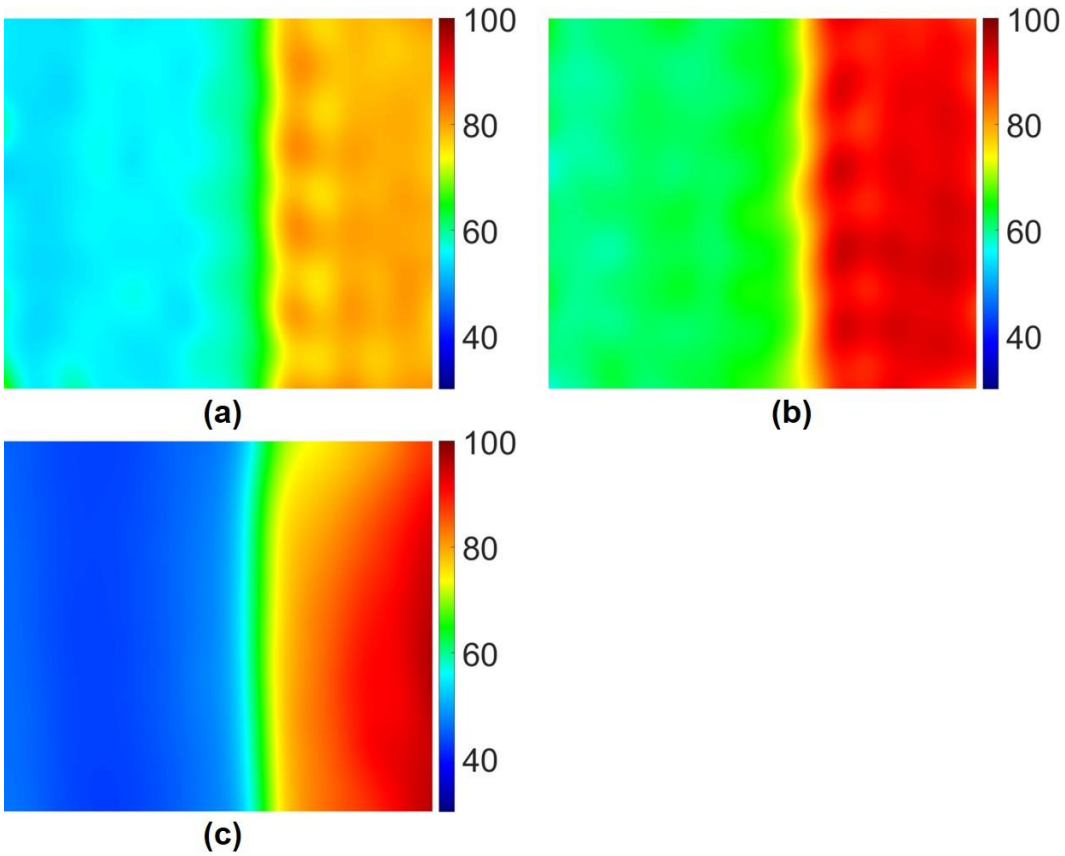

Fig. 3.9. Experimentally obtained temperature maps in K by analyzing fluorescence images taken by the top (a) or bottom (b) cameras. Experimentally obtained temperature map (c) in K for the same flow filed using NO PLIF two-line technique.

In addition, we acquired the planar laser induced fluorescence (PLIF) images of NO (1%) seeded in N_2 by probing NO (X $^2\prod_{1/2}$, υ" = 0) to measure temperature under the same flow conditions [47, 48]. Since there is no thermalization process in the NO PLIF, the temperature can reflect the true local flow temperature across the shock wave. We observed that the use of the VENOM technique resulted in an average temperature of 58 K in the pre-shock flow field, higher than the temperature obtained from NO PLIF by 14 K. The temperature measured downstream from the shock resulted in an average value of 85 K, showing a better agreement with NO PLIF temperature measurements with a deviation of 2 K. Since the gas density is higher after the shock, faster thermalization

through collisions is expected, resulting in smaller temperature overestimations in this region when using NO_2 photolysis–based VENOM.

3.4 Summary and Discussion

The NO_2 photolysis–based VENOM scheme intended for three-component velocity and planar temperature measurements was implemented. The velocity measurement using two approaches of "writing" grid, the micro-cylindrical lens array and aluminum mesh, both gave consistent results in three components. The overall velocity and temperature determinations followed the prediction. The measurements in the post-shock area showed a better agreement with the predicted values while there were relatively large deviations from the predictions in the pre-shock area. In particular, the streamwise motion determination in the pre-shock area using two tagging methods both gave the overestimation of velocity component by ~45 m/s compared with the previous value of 741 ± 2.3 m/s known from the nozzle characterization measurements. It was also higher than the value of 757 ± 8.0 determined by NO PLIF technique by 28 m/s. When the NO_2-seeded N_2 gas mixture at the stagnation temperature of 294 K was flowed through the Mach 6.2 nozzle into the chamber, the flow temperature rapidly dropped down to 34 K. Given the isentropic flow expansion, there is a possibility that NO_2 liquefaction contributed to faster flow speed than expected. It was previously reported that the experimental determination utilizing this NO_2 photolysis-based VENOM exceeded computational fluid dynamics (CFD) predictions in the low-density regions of the underexpanded jet [9]. An overestimation of the temperature resulted from probing a rotationally excited photoproduct to obtain rotational/translational temperature via the two-line thermometry technique [7, 8]. The subsequent studies showed that the insufficient collisional relaxation of the nascent NO photoproduct resulted in the temperature overestimation in low-density conditions even when the "write"-"read" pulses time delay was extended up to 2 μs [7]. In the meantime, when a high fraction of NO_2 is seeded and high-photolysis laser power is used, the photolysis of NO_2 can lead to thermal perturbation of the flow [29]. In summary, although the use of this VENOM technique shows the potential for accurate determinations of three-component velocity and planar temperature in high-speed flows, a solution to reduce the seeded condensation and thermal disturbance is necessary.

3.5 Simultaneous Velocity and Temperature Measurement Using NO

The technique presented in this section is a variant of the VENOM, as an alternative for tagging NO molecules produced by fluorescence and collisional quenching from the A $^2\Sigma^+$ state [29]. This tagging approach inherits the velocimetry advantages from the original VENOM technique, overcoming the short fluorescence lifetime of NO in highly quenching environments and providing discrimination from background NO. In addition, this new tagging method mitigates the possibility of thermal disturbance. Furthermore, the choice of seeding NO instead of NO_2 increase the compatibility of the VENOM technique with the current facilities where the use of NO_2 could be problematic due to condensation in low-temperature flow fields.

3.5.1 NO Vibrational Distributions

Following electronic excitation by the "write" laser at 226 nm, the A $^2\Sigma^+$ state NO molecules will relax back to the ground X $^2\prod$ state via either fluorescence or collisional quenching. The vibrational distribution of NO (X $^2\prod$) from A $^2\Sigma^+$ state fluorescence is governed by the Franck-Condon dominated vibrational transition probabilities which favor low vibrational states as seen in Fig. 3.10. The distribution peaks at v'' = 1 with 0.28 fractional yield. Since there are only NO and N_2 species, NO self-quenching and NO-N_2 quenching processes are taken into consideration. The quenching due to collisions with N_2 is negligible because the quenching cross sections are several orders of magnitude smaller than those of NO [49]. Hancock et al. has established that the collisional quenching is approximately statistical [44]. Rotational-level independence of collisional quenching of the A $^2\Sigma^+$ (v' = 0) state of NO has been previously proved, and thus the calculated recovery yields do not require rotational resolution. The vibrational distribution via collisional self-quenching is also shown in Fig. 3.10, displaying a long decaying tail from the low vibrational states to the higher vibrational states. The contributions of fluorescence and collisional quenching to the final vibrational distribution are determined by the ratios of intrinsic fluorescence decay and self-quenching rates [50]. Since the collisional quenching rates are temperature dependent, the final vibrational distribution is also temperature dependent. We have used a collision complex formation power-law model based on measurements by Setterson et al.[49], to calculate the self-quenching

cross sections at different temperatures. At the same time, the flow density and fraction of NO in the flow also affect the collisional quenching rates and hence the contribution of collisional quenching to the NO vibrational distribution. The vibrational distributions in the pre-shock and post-shock areas at temperatures of 34 K and 72 K are also shown in Fig. 3.10.

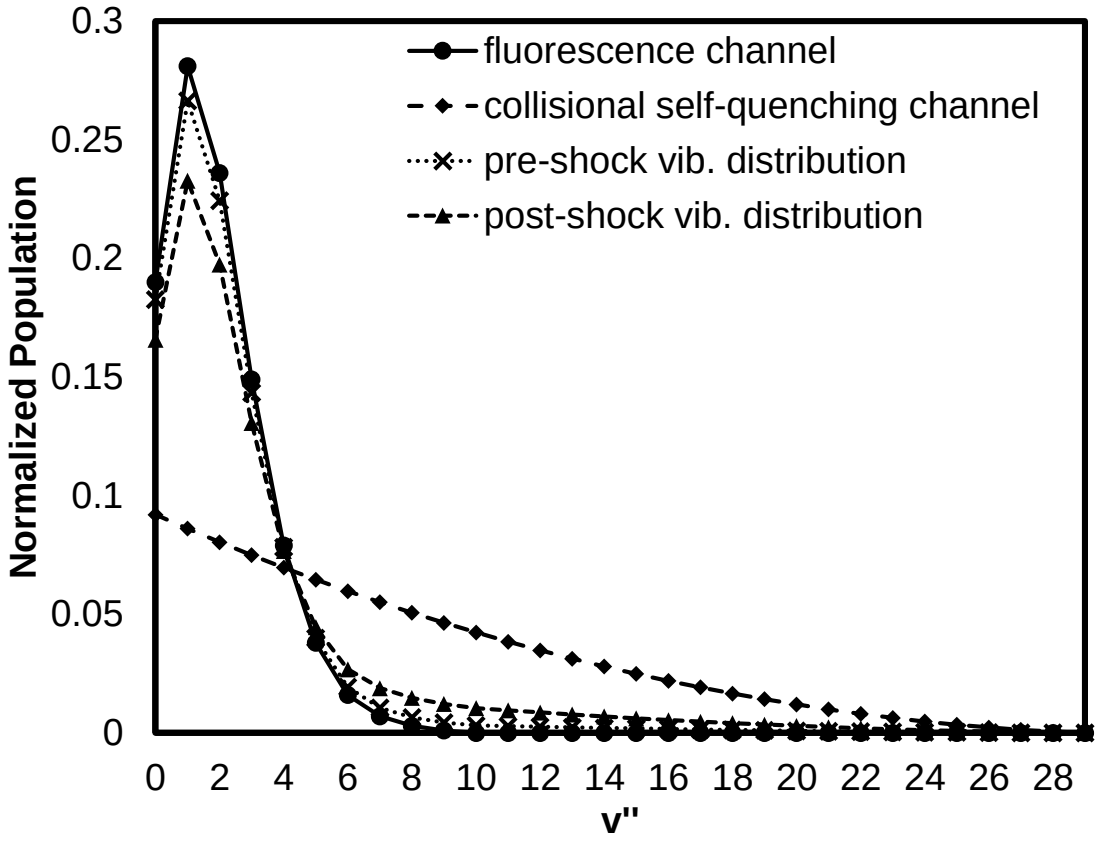

Fig. 3.10. Normalized vibrational distributions of NO (X $^2\Pi$) produced by fluorescence and collisional self-quenching channels, respectively, and by both channels in the pre-shock and post-shock areas.

After electronic excitation, the A $^2\Sigma^+$ fluorescence dominates the relaxation processes in the current ranges of pressure and temperature, resulting in similar vibrational distribution profile to the vibrational distribution produced via only A $^2\Sigma^+$ fluorescence. The fraction yield at v'' =1 in the post-shock region is lower than that in

the pre-shock area since the temperature and pressure increase across the oblique shock wave.

3.5.2 Simultaneous Measurement Using NO

Similar to the NO_2 photolysis-based VENOM experiments stated above, instead of seeding NO_2, the gas mixture, consisting of 5.0% NO in N_2 at a stagnation temperature of 294 K and pressure of 990 torr was flowed through the nozzle into the chamber to generate a pressure-matched and steady flow. The first PLIF laser system, used to "write" the MTV grid, was tuned to excite the $R_1 + Q_{21}$ band head of the A $^2\Sigma^+$ (υ' = 0) ← X $^2\prod_{1/2}$(υ" = 0) band near 226 nm, resulting in a grid of NO (υ" = 1) after spontaneous emission and collisional quenching from the A state. The "read" laser was sequentially tuned to probe the $R_1 + Q_{21}$ (8.5) and $R_1 + Q_{21}$ (1.5) transitions in the A $^2\Sigma^+$(υ' = 1) ← X $^2\prod_{1/2}$(υ" = 1) band, with time delays of 1200 ns and 1800 ns after the "write" laser. Following the same imaging processing procedure used in the previous section, the field-of-view corrected 100-shot average images are shown in Fig. 3.11. These images show a field of view of 13.0 × 8.1 mm with a spatial resolution of 59.1 pixels/mm. The effect of temperature and velocity variation across the shock is also clearly evident compared with the acquired fluorescence images using NO_2 photolysis-based VENOM technique.

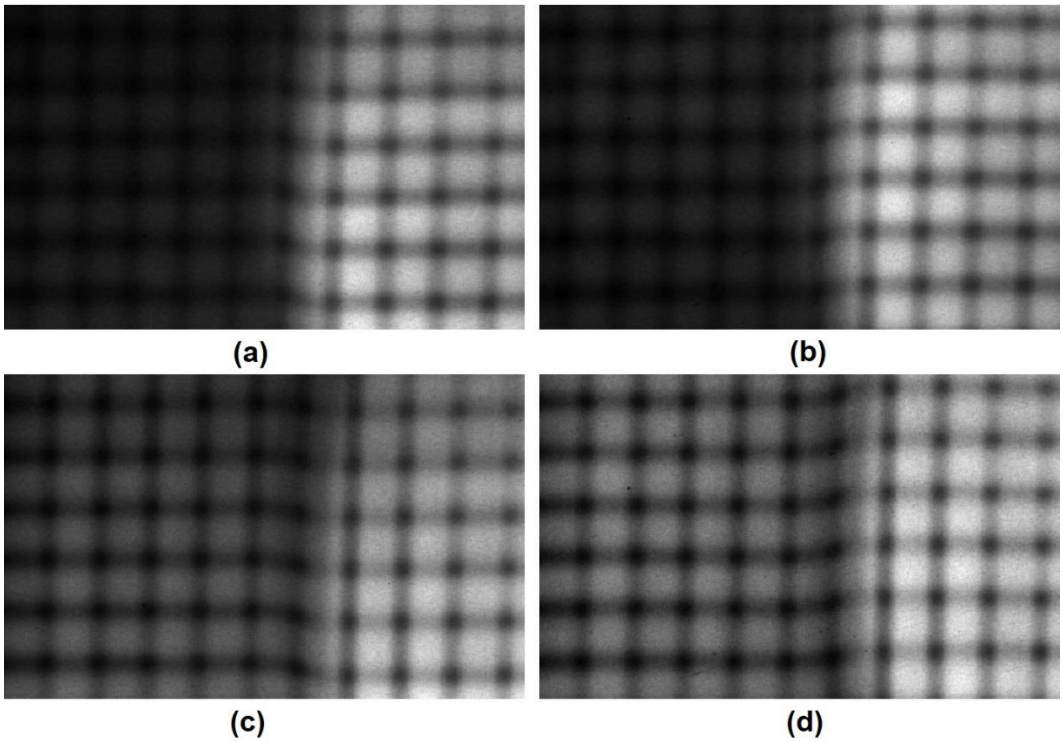

Fig. 3.11. Corrected 100-shot average (cropped) fluorescence images obtained with the top camera (a) probing J = 8.5 at a time delay of 1200 ns (c) probing J = 1.5 at a time delay of 1800 ns and acquired with the bottom camera (b) probing J = 8.5 at a time delay of 1800 ns.

The two field-of-view corrected time-delayed images acquired with each camera were employed to obtain local flow displacements at each grid intersection using 2D cross-correlation routines as stated above. Subsequently, three-component flow displacements were determined *via* geometric reconstruction based on the 2D displacements. The resulting velocity components are shown in Fig. 3.12, where the streamwise velocity component in the pre-shock area resulted in 755 ± 23 m/s within 2.2% deviation from the predicted value of 739 m/s, which is comparable to previous reports of streamwise motion determinations under similar conditions. The streamwise motion determination in the pre-shock shows a better agreement with the predicted value than that using NO_2 photolysis-based VENOM approach, partially supporting that the NO_2 condensation was contributing to the faster flow speed in that area. The post-shock

streamwise velocity component decreases to 645 ± 14 m/s, which is consistent with the calculated value of 648 ± 9 m/s, based on a wedge deflection angle of 17 ± 1 degrees. The out-of-plane velocity measurement in the post-shock resulted in a value of 150 ± 10 m/s, within 24% deviation from the expected value of 198 ± 10 m/s. There is a slightly decreasing trend in the out-of-plane component in the post-shock area. When the interrogation area is much close to the back edge of the plate, the flow will go beyond the edge, resulting in a decreasing out-of-plane component. The slightly larger deviation of the out-of-plane component from the expected value could be attributed to several factors that include the poor overlap between the MTV grid and probe laser sheet as well as uncertainty in the wedge angle measurement leading to error in the assumed flow conditions. The out-of-plane velocity component before the shock wave is consistent with the expected value of 0 m/s, while the radial velocity component is negligible as predicted in both pre-shock and post-shock areas, as shown in Fig. 3.12. The overall velocity measurement is consistent with the predicted velocity profile.

The utilization of the aluminum mesh for this tagging purposes also leads to a modulation of the excitation “write” pattern, permitting a temperature determination. The fluorescence images were acquired by probing the two rotational states with the same time delays (1200 ns or 1800 ns) to obtain temperature maps without de-warping the second time-delayed image back onto the first one using velocity measurement results.

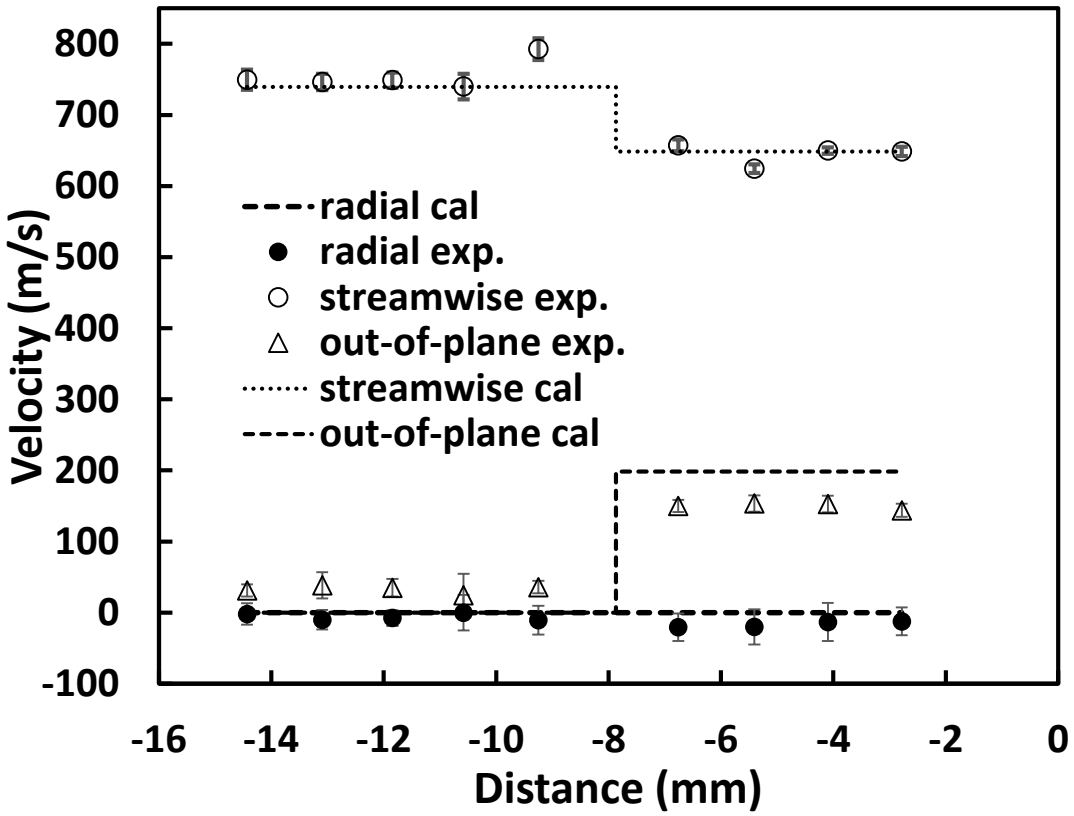

Fig. 3.12. Experimentally determined streamwise, out-of-plane, and radial velocity components in the Mach 6.2 flow field across the oblique shock. The predicted velocity components are shown for comparison.

This process also allows calculation of fluorescence ratios that correspond to the same flow elements. Temperature measurements using the VENOM technique are based on two-line thermometry and thus require a thermalized rotational distribution of the NO (X $^2\Pi$, v" = 1) to reflect the true local flow temperature. The initial rotational distribution in the A $^2\Sigma^+$ (v' = 0) state generated by the "write" laser beam reflects the selective excitation of a small range of low-J transitions associated with the band head [29]. Following excitation by the "write" laser, NO molecules in the A $^2\Sigma^+$ state undergo rotational energy transfer (RET) by collision with ground state NO and N_2. Rotational thermalization in the NO (X $^2\Pi$, υ") states is completed within a few hundred nanoseconds at a few hundred Pa for high-speed flows [8, 9]. The chosen time delays, therefore, permit enough time for the

completion of rotational thermalization. The temperature maps by analyzing J = 8.5 and J = 1.5 fluorescence images obtained with the same camera at the same time delay are shown in Fig. 3.13.

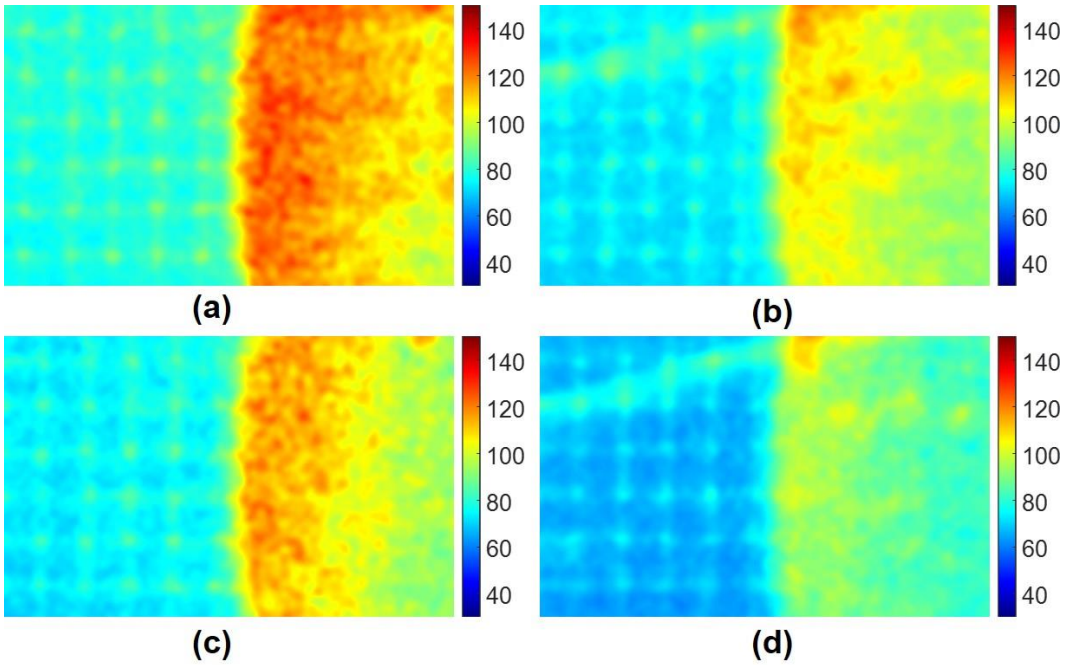

Fig. 3.13. Experimentally obtained temperature maps in Kelvin by analyzing J = 8.5 and J = 1.5 fluorescence images taken by the top (a and c) or bottom (b and d) cameras at the time delays of 1200 ns and 1800 ns.

According to the temperature maps in Fig. 3.13, the temperatures in both pre-shock and post-shock areas are much higher than expected. In particular, the temperature in the pre-shock region is higher than the predicted value by ~40 K. The temperature determination at the second time delay of 1800 ns shows a slightly lower average temperature than that determined at the time delay of 1200 ns. This negligible temperature change also supports the fact that the rotational thermalization is completed within the chosen time delays. In the meantime, there is a weak dependence of the measured temperature on the position of the cameras in the post-shock region.

The tagging efficiency was calculated for this mixture of 5% NO in N_2. The NO absorption cross-section at 226 nm is 1.426×10^{-19} m^2. The efficiency was estimated assuming a 226 nm beam with an exit diameter of 9 mm expanded to a diameter of 2 cm before being formed into a 200 μm thickness sheet. The ~5% of the seeded NO was estimated to be excited to A $^2\Sigma^+$ (v' = 0) state with a laser power of ~12 mJ/pulse. When the A $^2\Sigma^+$ (v' = 0) NO molecules return to the ground X $^2\Pi$ state, a fraction of the energy will be partitioned into rotation and translation via collisional quenching, resulting in the rotational/translational temperature rise. The fraction of NO in N_2 affects the quenching rates and hence the temperature rise depends on the fraction of NO.

3.5.3 Seeding Fraction Effect

In order to investigate the effect of NO fraction on the temperature determination, the gas mixtures of 10% and 1% NO in N_2 were flowed through the same nozzle into the chamber. Then, the temperature measurements by a global fit of LIF excitation spectrum were conducted, respectively. The aluminum mesh was removed to allow collecting fluorescence images with full intensity pattern. The "read" laser system was tuned to probe the NO (1, 1) band transitions at the time delay of 1200 ns after the "write" laser. The fluorescence images were recorded by an Andor iStar DH734 ICDD camera aligned normal to the imaging plane with a gate width of 100 ns. The LabView program intended for the dye laser calibration was modified to synchronize the camera with the "read" laser system to acquire fluorescence images at each wavelength in the range of ~223 – 224 nm required for excitation of the NO (1, 1) gamma band. The camera was trigged at 0.5 Hz to record a fluorescence image at each wavelength with a step size of 0.0006 nm. Fig. 3.14 shows a fluorescence image at a certain wavelength. The blue area in the image represents the pre-shock region while the high-intensity area is the post-shock region. The fluorescence counts within the red rectangular areas were averaged to obtain the pre-shock and post-shock fluorescence intensity at this specific wavelength, respectively. Repeating this image averaging at every wavelength position resulted in the LIF spectrums within the chosen wavelength range. A global fit of experimentally determined spectrum was run with respect to the simulation spectrum that was generated with a resolution of 0.0025 nm using LIFBASE program. When the best fit was reached, the temperature was determined in that area.

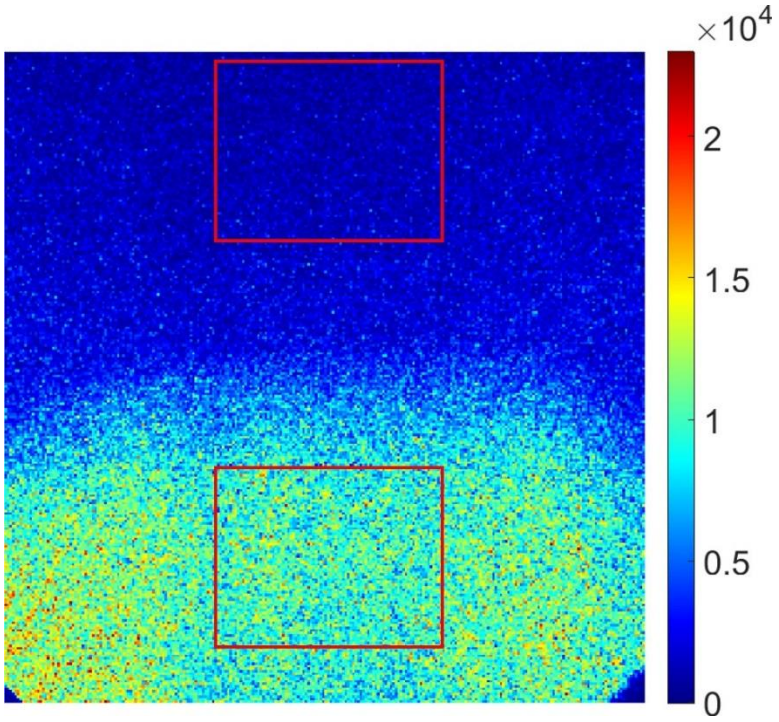

Fig. 3.14. Full-frame fluorescence image acquired with the Andor iStar ICCD camera at a certain wavelength.

The top panel in Fig. 3.15 displays the fit of the LIF spectrum in the pre-shock region that includes most of resolvable branches of NO (1, 1) band when the gas mixture of 10% NO in N_2 was flowed through the nozzle. The lower signal-to-noise levels in this area resulted in some fluctuations in the experimental spectrum though the LIF spectrums were averaged over three scanning cycles. The temperature was estimated to be 85 K, higher than the predicted value under the flow condition, but is consistent with the result determined using two-line thermometry technique in this section. The bottom panel represents the fit in the post-shock region, which shows a smoother experimental PLIF spectrum due to better signal-to-noise ratio in this area. This fit resulted in a temperature

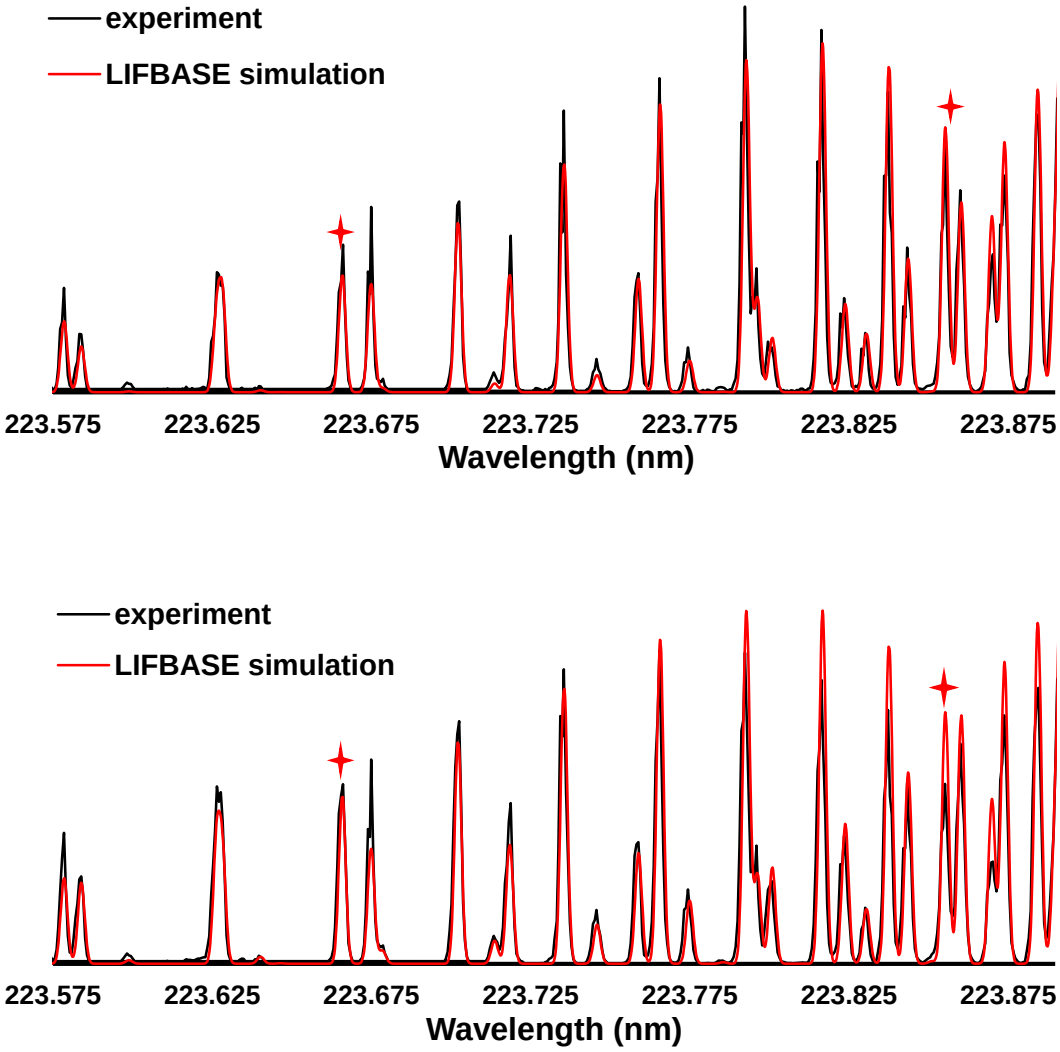

Fig. 3.15. The global fits of the experimentally determined LIF spectrums acquired by seeding 10% NO with respect to the simulated at temperatures in the pre-shock (top panel) and post-shock (bottom panel) regions. The read crosses indicate where the chosen two lines used in the two-line thermometry scheme are.

of 105 K, higher than the expected value of 72 K, in agreement with the result by two-line thermometry measurement. Since each fluorescence image was acquired at a specific wavelength, quite different from ensemble images acquisition by probing two lines, the intensity is sensitive to both “write” and “read” laser shot-to-shot power variation. The

"read" laser power was monitored and recorded *via* the program which was used to correct the fluorescence intensity. However, the "write" laser power was difficult to be accounted for. The scanning can be repeated to acquire more images set to decrease uncertainty at the expense of an increase of gas use and elongated images acquisition times.

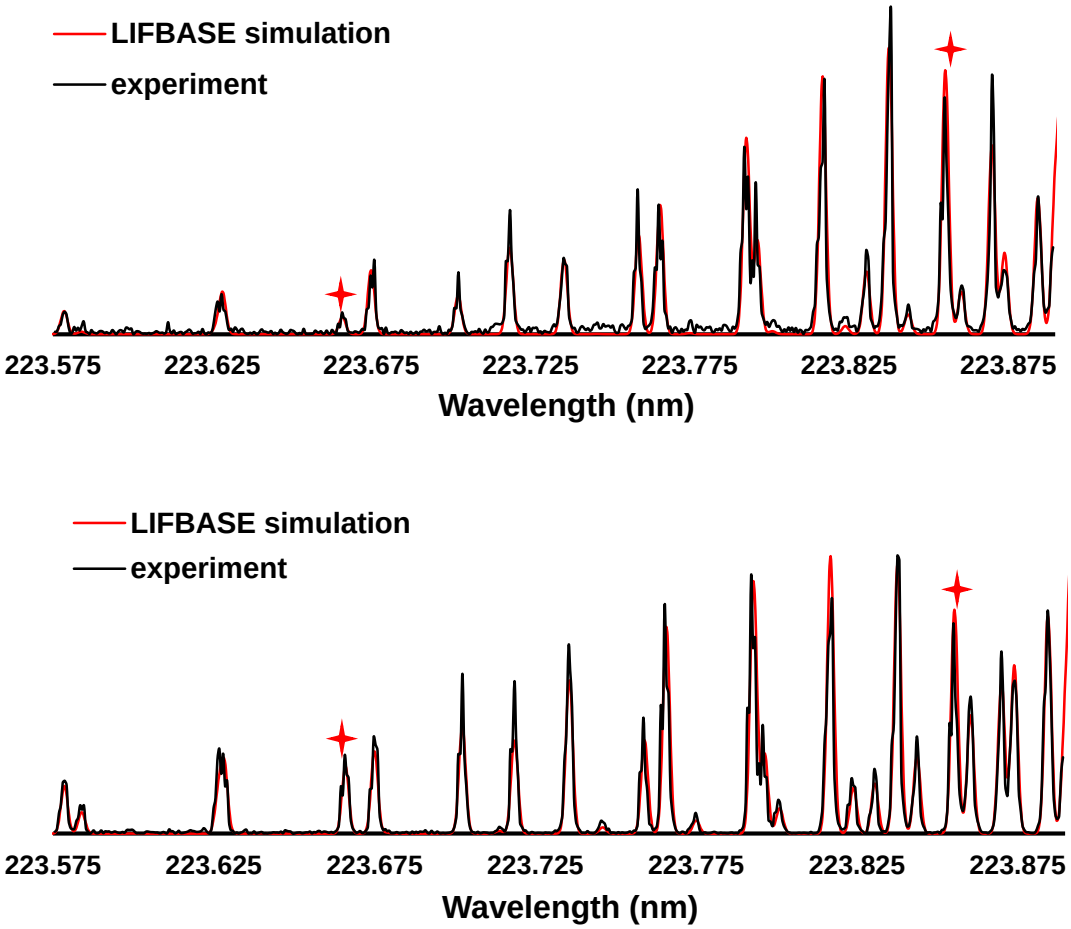

Fig. 3.16. The global fits of the experimentally determined LIF spectrums acquired by seeding 1% NO with respect to the simulated at temperatures in the pre-shock (top panel) and post-shock (bottom panel) regions. The read crosses indicate where the chosen two lines used in the two-line thermometry scheme are.

The temperature determination with a full scan of absorption lines in this study by seeding higher fraction of NO can indeed result in the rotational/translational temperature rise. In order to further interrogate this effect, the gas mixture of 1% NO in N_2 was tested under the same conditions above. Figure 3.16 displays the two PLIF fits in both pre-shock and post-shock regions. Both experimental PLIF spectrums are fitting well with the simulated spectrums at the determined temperatures. On the one hand, the fit in the pre-shock area gives a temperature value of 45 K when the experimental spectrum was fitted with the simulated in most of resolvable absorption lines, in which a tiny fluorescence peak is shown in the J = 8.5 line. On the other hand, the post-shock fit results in a temperature of 72 K which is consistent with the predicted value of 72 ± 4 K. Hence, tagging a low fraction of NO can avoid the temperature rise resulting from the collisional quenching in the tagging process even though a higher fraction of NO can probably lead to more fluorescence signal.

Given the conclusion above that a high NO seeding fraction can result in the rotational/translational temperature rise, a gas mixture of 2% NO in N_2 was used to obtain simultaneous measurement of three-component velocity and planar temperature. All the test conditions were kept same except the NO fraction. The corrected 540-shot average fluorescence images at the time delays of 1200 ns and 1800 ns showing the area of interest across the oblique shock are shown in Fig. 3.17. The flow is from the left to right and the images with a spatial resolution of 46.5 pixels/mm, display an area of 11.6 × 6.5 mm.

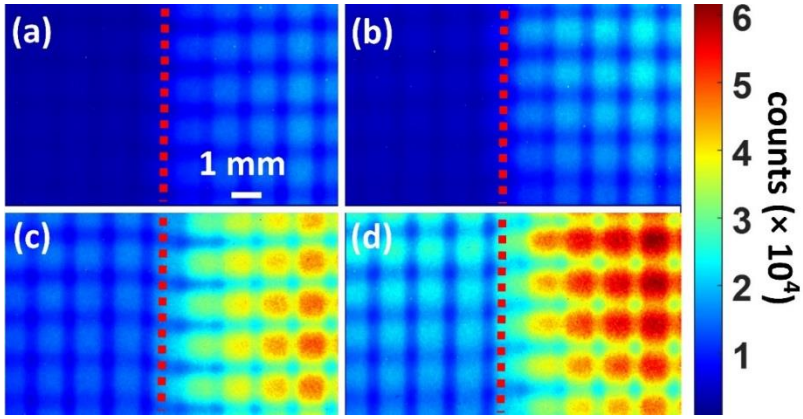

Fig. 3.17. PLIF images (cropped) acquired with the top camera (a) probing J = 8.5 at a time delay of 1200 ns (c) probing J = 1.5 at a time delay of 1800 ns. PLIF images (cropped) acquired with the bottom camera (b) probing J = 8.5 at a time delay of 1200 ns (d) probing J = 1.5 at a time delay of 1800 ns. The red dashed line indicates the position of the shock wave [8].

The two field-of-view corrected time-delayed images presented above were employed to obtain local flow displacements at each grid intersection using 2D cross-correlation routines. Then, three-component flow displacements were determined in the same way stated previously. The resulting velocity component plots are shown in Fig. 3.18 (left panel), where the streamwise velocity component in the pre-shock area resulted in 760 ± 14 m/s within 2.8% deviation from the predicted value of 739 m/s, which is comparable to previous reports of streamwise motion determinations under similar conditions. The post-shock streamwise velocity component decreases to 672 ± 20 m/s, which is consistent with the calculated value of 657 ± 9 m/s, based on a wedge deflection angle of 16 ± 1 degrees. The out-of-plane velocity measurement in the post-shock resulted in a value of 169 ± 8 m/s, within 10% deviation from the expected value of 188 ± 10 m/s. The out-of-plane velocity component before the shock wave is consistent with the expected value of 0 m/s, while the radial velocity component is negligible as predicted in both pre-shock and post-shock areas, as shown in Fig. 3.18. The overall velocity profile follows the predicted velocity components calculated based on the measured wedge angle.

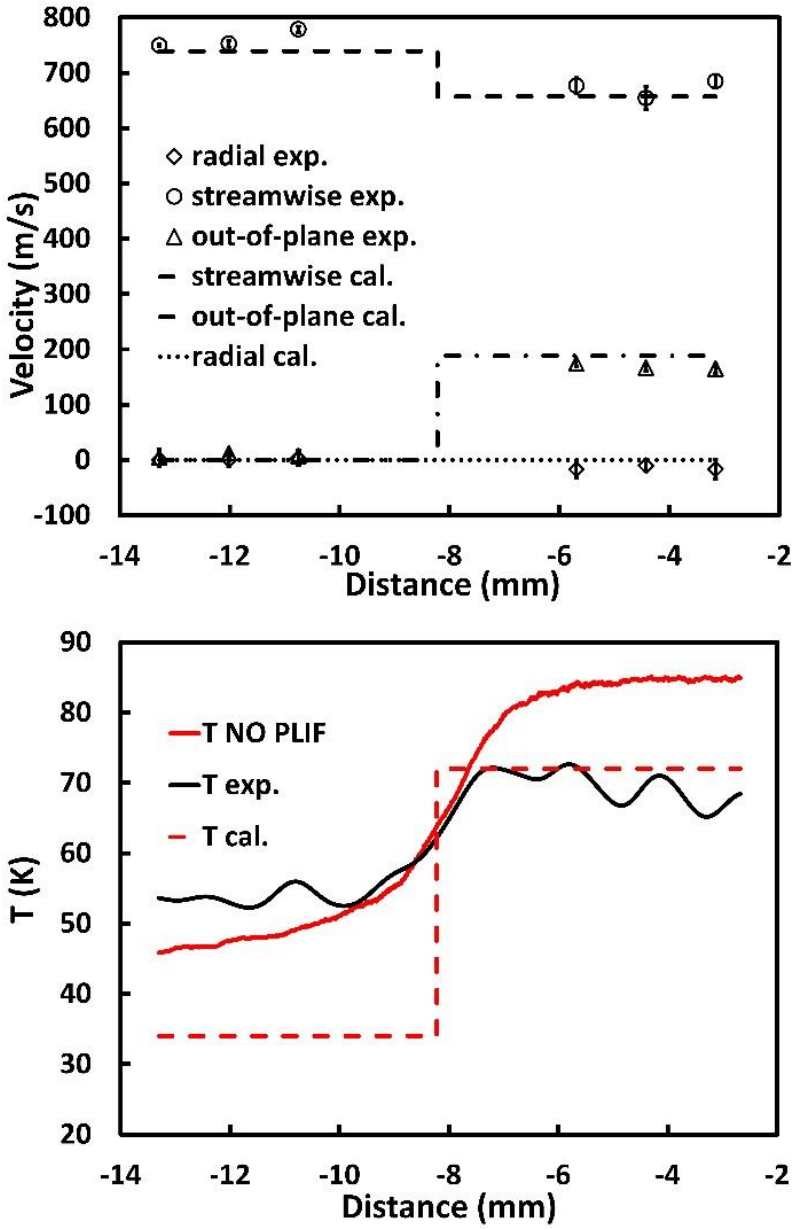

Fig. 3.18. Experimental obtained three-component velocity (upper panel). The predicted velocity components are shown for comparison. Bottom panel shows the temperature experimentally determined using the VENOM technique and NO PLIF two-line thermometry, and predicted temperature profile [8].

The 2D MTV measurement provides enough displacement information to de-warp the second time-delayed image onto the first one acquired by each camera, allowing

calculation of fluorescence ratios that correspond to the same flow elements. Since temperature measurements using this VENOM technique are also based on two-line thermometry and thus require a thermalized rotational distribution of the NO ($X\ ^2\Pi$, v'' = 1) to reflect the true local flow temperature. Rotational thermalization in the NO ($X\ ^2\Pi$, v'') states is completed within a few hundred nanoseconds at a few hundred Pa for high-speed flows. The chosen time delays, as seen above, permit enough time for the completion of rotational thermalization. Two independent temperature measurements were obtained by analysis of the VENOM image pairs acquired using the top and bottom cameras. We observed no dependence of the measured temperature on the position of the cameras. In addition, temperature measurements with reversed probing images (the J = 1.5 image at 1200 ns and J = 8.5 image at 1800 ns) showed consistent results, suggesting that out-of-plane flow motion during the time delay between the two "read" events did not lead to a decreased overlap between the tagged grid and probe laser sheet. Thus, the laser sheet thickness (approximately 200 μm) and its effect on fluorescence intensities is a negligible factor. The bottom panel in Fig. 3.18 displays the determined temperature profile in the area of interest from the two time-delayed images of the top and bottom cameras. In addition, we acquired planar laser induced fluorescence (PLIF) images of NO (1%) seeded in N_2 by probing two rotational states of NO ($X\ ^2\Pi$, v'' = 0) to determine temperature under the same flow conditions. The stereoscopic VENOM measurements resulted in an average temperature of 54 K in the pre-shock area, as shown in Fig. 3.18, 6 K higher than the temperature obtained from NO PLIF and 20 K higher than the freestream temperature of 34.0 ± 0.4 K known from nozzle characterization measurements [4]. Although the observed temperature discrepancies could be potentially attributed to a variety of factors that include thermal effects from the tagging process, previous studies using this tagging approach in a low-temperature, low-density, flow field did not show systematic temperature overestimation within similar timescales [29]. However, the temperature measured downstream from the shock resulted in a value of 69 K with a spatial uncertainty of 2 K, showing a better agreement with the predicted temperature of 72 ± 4 K. The gradual increase in the measured temperature profiles observed across the shock using VENOM and NO PLIF can be attributed not only to spatial averaging given the flow displacement during the employed time delay between the two "read" events and potential shock variations originating from

pulse-to-pulse fluctuations, but also to probing sheet thickness. Since the gas density and temperature is lower before the shock, lower fluorescence signal and hence lower signal-to-noise ratio result in larger discrepancies in the temperature determined in this region using the VENOM technique. The observed discrepancies between the temperature measurements obtained using VENOM, NO PLIF and those expected from calculations could be attributed to a variety of factors that include unaccounted laser and absorption line overlap as well as uncertainty in the wedge angle measurement leading to error in the assumed flow field conditions. A comprehensive error analysis of VENOM measurements including the use of NO PLIF thermometry has previously been performed [7, 8]. The overall temperature measurement, however, is consistent with the predicted temperature profile. Although the resolution of the optical system of 76 μm, determined by measuring the modulation transfer function, represents the resolution limit of the technique, the magnitude of the local flow displacements limits the practical spatial resolution of the velocity and temperature determinations. Local flow displacements in the current experiments resulted in spatial resolutions of 403 μm and 101 μm along the streamwise and out-of-plane directions, respectively.

3.6 Summary

The variant of the VENOM technique that employs NO (v'' = 1) resulting from spontaneous emission and collisional quenching from the A $^2\Sigma^+$ (v' = 0) NO molecules, was used to obtain the simultaneous measurement of three-component velocity and planar temperature in the same flow field studied in Section 3.3. Compared to NO_2 photolysis-based VENOM method, the choice of seeding NO avoids the condensation issue inherent in the use of NO_2, and also mitigates the possibility of thermal disturbance. The "write" laser beam generates a selective excitation of a small range of NO low-J transitions associated with the band head. After excitation, these A $^2\Sigma^+$ (v' = 0) NO molecules undergo RET by collision. The studies by Ebata et al. established that RET rates could result in the completion of rotational thermalization within tens of nanosecond at pressures of a few hundred Pa [51]. This tagging approach has showed a better agreement in temperature measurement in low-density, low-temperature regions of the underexpanded jet with CFD simulation than previous studies via NO_2 photodissociation VENOM technique.

The velocity measurement displays more comparable results to the predictions than those obtained via NO_2 photodissociation approach, particularly in the determination of the streamwise component in the pre-shock region. The effect of NO seeding fraction on temperature determination was investigated by flowing the gas mixtures of 10% and 1% NO/N_2 through the Mach 6.2 nozzle into the chamber, respectively. It was found that a high seeding fraction resulted in a rotational/translational temperature rise in the tagging process due to collisional quenching from the $A\ ^2\Sigma^+$ (v' = 0) state. The more NO is seeded into the flow, the higher the estimated temperature will be. Hence, an accurate temperature determination using two-line thermometry can be obtained at the expense of low signal-to-noise levels when studying extremely cold high-speed flows where spontaneous emission does not dominate the relaxation processes of the $A\ ^2\Sigma^+$ (v' = 0) state NO molecules. A higher "write" laser power is necessary to achieve good signal-to-noise ratio since it can enable higher excitation efficiency and thus increase the percentage of NO (v'' = 1).

4. CONCLUSION AND FUTURE WORK

4.1 Instantaneous Fluctuations Measurement

The VENOM experiments performed in the flow field described in the third section employs a “write” laser to tag the flow field with NO (v’’ =1) and a “read” laser that was tuned to sequentially probe specific rotational lines at time delays of ~1 μs after the “write” laser. Although the three-component velocity and planar temperature of the flow field were simultaneously determined by analyzing the sequential fluorescence image pairs, the measurements provided uncorrelated velocity and temperature information due to the uncorrelated two probing events. Specifically, the two probing events followed different “writing” laser pulses. This timing schematic can provide a relatively accurate measurements in steady flow fields, but fails to determine instantaneous fluctuations in such unsteady flow fields as highly turbulent flows. Since the characteristic time of turbulent flows is in the microsecond time scale, the instantaneous measurements should be conducted within sub-microsecond time scale to characterize the turbulence.

The simultaneous use of one “write” laser and two “read” lasers can enable instantaneous single-shot measurements of velocity and temperature fields using the VENOM technique. This simultaneous and instantaneous measurement has been previously demonstrated in two-component velocity and temperature determinations of an underexpanded jet and cylinder downstream wake flow using two synchronized Andor iStar ICCD cameras [7, 8]. The field of view of the second time-delayed image was de-warped back onto the first one, which allowed the simultaneous determination of temperature fields. The dual image feature (DIF) of the two cameras used in the present study enables double-shutter cameras imaging. This feature can help us capture sequential image pair by tuning the internal recording time delay in rapid succession. Hence, the cameras in the stereoscopic configuration can be synchronized to two “read” lasers using DIF to record time-delayed images following the two “read” lasers. Each single-shot image pair can provide the instantaneous determinations of three-component velocity and planar temperature, resulting in the measurement of both velocity and temperature fluctuations. The investigation of instantaneous fluctuations in velocity and temperature will shed light on the energy flux in the given flow fields, which will pave the

way for the studies of high-speed turbulent flows. This experimental setup is shown in Fig. 4.1.

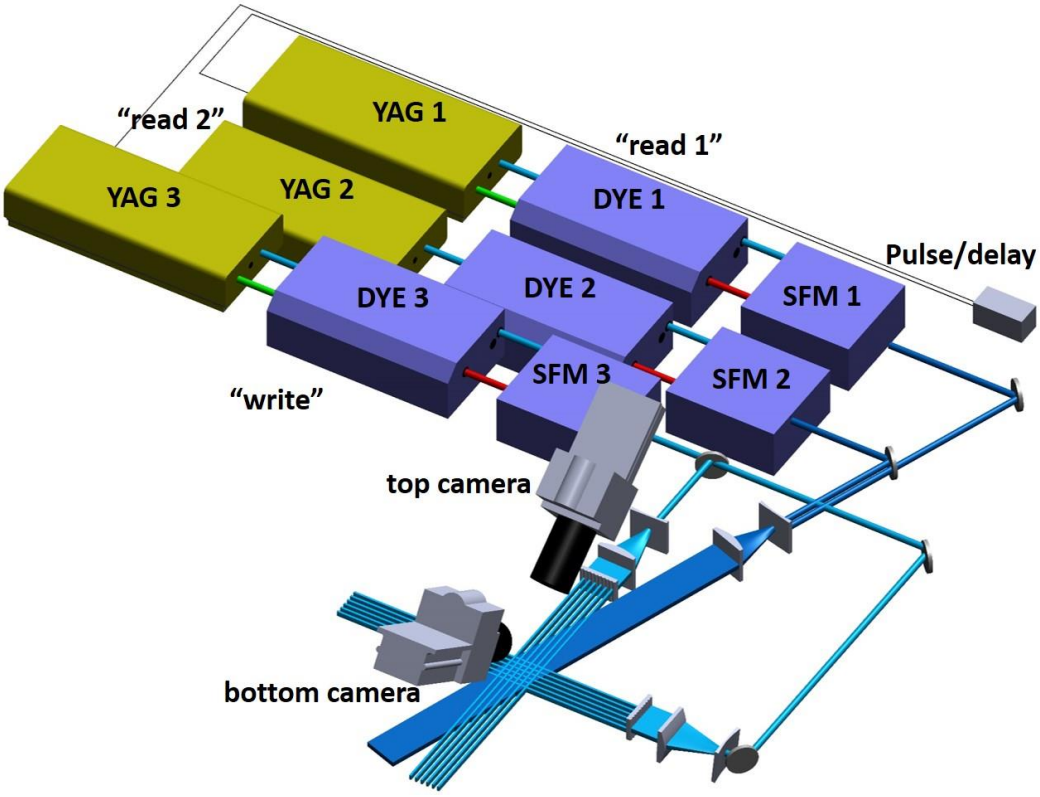

Fig. 4.1. Schematic of one "write" and two "read" laser systems.

4.2 Limitations Study and Application Expansion

The NO-seeded stereoscopic VENOM technique is primarily applied to the study of cold high-speed flow fields in this thesis. Recently, we have obtained one-dimensional (1D) velocity measurement in turbulent boundary layer via the VENOM technique on the high-speed, high Reynolds number wind tunnel. Fig. 4.2 shows the overlay of PLIF images acquired at two time delays. This VENOM technique allows us to obtain more accurate velocity measurement in the flow field with a prohibitive degree of light scattering near an object surface where PIV technique suffers from non-uniform particle seeding and inaccuracies in tracking velocity.

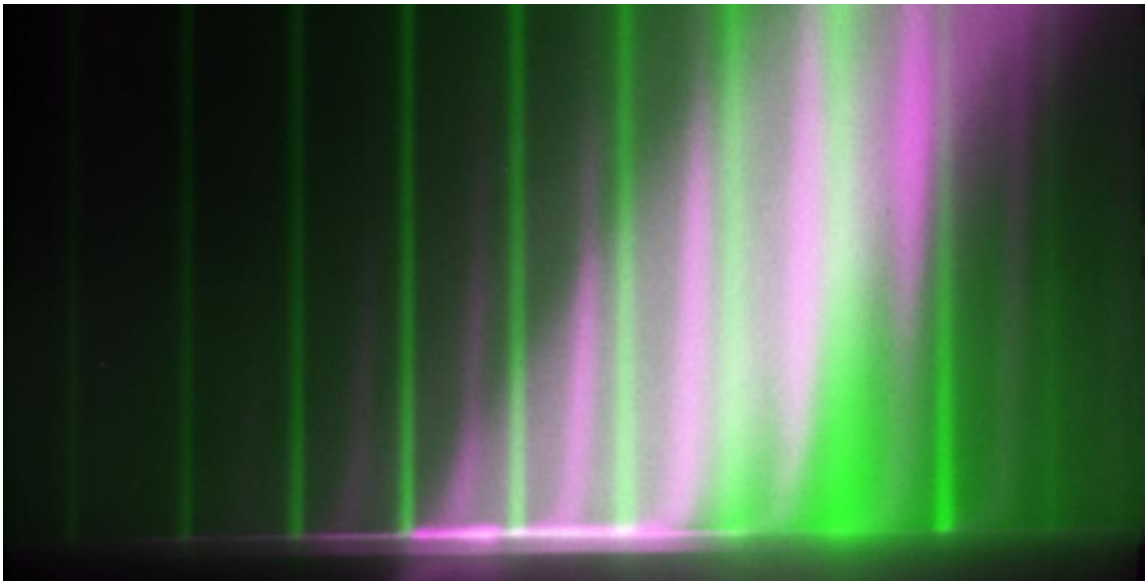

Fig. 4.2. The overlay of PLIF images acquired at time-zero (green lines) and 2000 ns delay.

The technique shows the potential for three-dimensional velocimetry measurement in high speed flows, but suffers from temperature overestimation in the cold flow field with high NO seeding fraction due to collisional quenching. According to the experiments stated in Section 3.4.3, the temperature determination in the cold flow field is sensitive to this seeding effect. Further work on this VENOM technique will be needed to assess limitations by applying it to different flow fields that include but are not limited to high-enthalpy, or high-density flows.

Since the vibrational relaxation is much slow within the measurement time scale, the vibration-rotation (V-R), vibration-translation (V-T) and vibration-vibration (V-V) energy exchange processes of flow species are not accounted for in the temperature measurement. However, these processes are nontrivial compared to rotation-translation energy exchange in high-temperature (~1000 K) flow fields. A theoretical model has been recently developed to simulate the vibrational relaxation. This model takes into consideration the V-R, V-T and V-V processes and trace the NO vibrational population after tagging event versus time. Not only can the model provide the time-dependent vibrational distribution of NO under different flow conditions but also the rotational/translational temperature rise due to energy exchange. The vibrational

temperature can be obtained by assuming a Gaussian fit to the simulated vibrational population. Hence, experimental studies of vibrational relaxation are necessary to map out the vibrational temperature and verify the theoretical model.

Experimentally, the NO vibrational temperature can be obtained by probing the populations of the two vibrational levels of NO simultaneously using NO PLIF. Thus, the vibrational temperature decay of NO can be temporally tracked. Similar to the rotational/translational temperature determination, the fluorescence signal is collected in the linear fluorescence regime by probing two different vibrational levels and identical rotational states. The fluorescence signal is a complicated function of the initial population of the probed state, the ratio of the stimulated emission Einstein coefficients, the saturation and laser intensities, the spontaneous emission Einstein coefficient, and an overall efficiency term which is combined as a constant C_{12}. As stated above, the quenching cross sections are not dependent on initial vibrational states. The quenching rates in the excited A state are nearly equal for the ground (v = 0) and excited vibrational level (v = 1).

$$R_{12} = \frac{S_{f1}}{S_{f2}} = C_{12} e^{-\Delta E_{vib}/kT_{vib}} \qquad \text{(Eq. 4.1)}$$

As a result, collecting NO fluorescence by probing two different vibrational states at different time delays after the “write” laser and calculating the fluorescence ratio using Eq. 4.1 can determine the vibrational temperature map of the given flow field.

REFERENCES

1. A. J. Favre, "The equations of compressible turbulent gases," AD622097 (Institut de Mecanique Statistique de la Turbulence, Marseille, France, 1965).

2. S. Brennan, "Blue cigarette smoke" (2008), retrieved 04/08/2016, 2016, https://www.flickr.com/photos/weeping-willow/2728104739/in/photostream/.

3. R. E. Ecke, "The turbulence problem: An experimentalist's perspective," Los Alamos Science (2005).

4. R. Sánchez-González, R. Srinivasan, J. Hofferth, D. Y. Kim, A. J. Tindall, R. D. W. Bowersox, and S. W. North, "Repetitively pulsed hypersonic flow apparatus for diagnostic development," AIAA Journal **50**, 691-697 (2012).

5. A. Hsu, "Application of advanced laser and optical diagnostics towards non-thermochemical non-equilirium systems," Ph.D. dissertation (Texas A&M University, 2009).

6. A. G. Hsu, R. Srinivasan, R. D. W. Bowersox, and S. W. North, "Two-component molecular tagging velocimetry utilizing NO fluorescence lifetime and NO_2 photodissociation techniques in an underexpanded jet flowfield," Appl. Opt. **48**, 4414-4423 (2009).

7. R. Sánchez-González, "Advanced laser diagnostics development for the characterization of gaseous high speed flows," Ph.D. dissertation (Texas A&M University, 2012).

8. R. Sánchez-González, R. D. W. Bowersox, and S. W. North, "Simultaneous velocity and temperature measurements in gaseous flowfields using the vibrationally excited nitric oxide monitoring technique: a comprehensive study," Appl. Opt. **51**, 1216-1228 (2012).

9. R. Sánchez-González, R. Srinivasan, R. D. W. Bowersox, and S. W. North, "Simultaneous velocity and temperature measurements in gaseous flow fields using the VENOM technique," Opt. Lett. **36**, 196-198 (2011).

10. F. Pan, R. Sánchez-González, M. H. McIlvoy, R. D. W. Bowersox, and S. W. North, "Simultaneous three-dimensional velocimetry and thermometry in gaseous flows using the stereoscopic vibrationally excited nitric oxide monitoring technique," Opt. Lett. **41**, 1376-1379 (2016).

11. J. N. Forkey, N. D. Finkelstein, W. R. Lempert, and R. B. Miles, "Demonstration and characterization of filtered Rayleigh scattering for planar velocity measurements," AIAA Journal **34**, 442-448 (1996).

12. R. J. Exton and M. E. Hillard, "Raman Doppler velocimetry: a unified approach for measuring molecular flow velocity, temperature, and pressure," Appl. Opt. **25**, 14-21 (1986).

13. D. Most and A. Leipertz, "Simultaneous two-dimensional flow velocity and gas temperature measurements by use of a combined particle image velocimetry and filtered Rayleigh scattering technique," Appl. Opt. **40**, 5379-5387 (2001).

14. P. S. Kothnur, M. S. Tsurikov, N. T. Clemens, J. M. Donbar, and C. D. Carter, "Planar imaging of CH, OH, and velocity in turbulent non-premixed jet flames," Proc. Combust. Inst. **29**, 1921-1927 (2002).

15. G. H. Park, D. Dabiri, and M. Gharib, "Digital particle image velocimetry/thermometry and application to the wake of a heated circular cylinder," Exp. Fluids **30**, 327-338.

16. J. Rehm, N. Clemens, J. Rehm, and N. Clemens, "A PIV/PLIF investigation of turbulent planar non-premixed flames," in *35th Aerospace Sciences Meeting and Exhibit,* (American Institute of Aeronautics and Astronautics, Reno, NV, 1997).

17. H. Richard and E. Gregory, "An experimental investigation of accurate particle tracking in supersonic, rarefied, axisymmetric jets," in *47th AIAA Aerospace Sciences Meeting including The New Horizons Forum and Aerospace Exposition,* (American Institute of Aeronautics and Astronautics, Orlando, FL, 2009).

18. J. Sakakibara, K. Hishida, and M. Maeda, "Vortex structure and heat transfer in the stagnation region of an impinging plane jet (simultaneous measurements of velocity and temperature fields by digital particle image velocimetry and laser-induced fluorescence)," Int. J. Heat Mass Transfer **40**, 3163-3176 (1997).

19. M. Tsurikov and N. Clemens, "Scalar/velocity imaging of the fine scales in gas-phase turbulent jets," in *39th Aerospace Sciences Meeting and Exhibit,* (American Institute of Aeronautics and Astronautics, Reno, NV, 2001).

20. T. Sakurai, T. Handa, S. Koike, K. Mii, and A. Nakano, "Study on the particle traceability in transonic and supersonic flows using molecular tagging velocimetry," J. Vis. **18**, 511-520 (2015).

21. H. Hui and M. K. Manoochehr, "Molecular tagging velocimetry and thermometry and its application to the wake of a heated circular cylinder," Meas. Sci. Technol. **17**, 1269 (2006).

22. M. R. Edwards, A. Dogariu, and R. B. Miles, "Simultaneous temperature and velocity measurements in air with femtosecond laser tagging," AIAA Journal **53**, 2280-2288 (2015).

23. W. Christian, "Stereoscopic digital particle image velocimetry for application in wind tunnel flows," Measurement Science and Technology **8**, 1465 (1997).

24. H. Hui, "Stereo particle imaging velocimetry techniques," in *Handbook of 3D Machine Vision* (Taylor & Francis, 2013), pp. 71-100.

25. N. J. Lawson and J. Wu, "Three-dimensional particle image velocimetry: error analysis of stereoscopic techniques," Meas. Sci. Technol. **8**, 894 (1997).

26. G. D. Bohl, M. M. Koochesfahani, and J. B. Olson, "Development of stereoscopic molecular tagging velocimetry," Exp. Fluids **30**, 302-308 (2001).

27. S. Krüger and G. Grünefeld, "Stereoscopic flow-tagging velocimetry," Appl. Phys. B **69**, 509-512 (1999).

28. M. Mittal, R. Sadr, H. J. Schock, A. Fedewa, and A. Naqwi, "In-cylinder engine flow measurement using stereoscopic molecular tagging velocimetry (SMTV)," Exp. Fluids **46**, 277-284 (2008).

29. R. Sánchez-González, R. D. W. Bowersox, and S. W. North, "Vibrationally excited NO tagging by NO (A $^2\Sigma^+$) fluorescence and quenching for simultaneous velocimetry and thermometry in gaseous flows," Opt. Lett. **39**, 2771-2774 (2014).

30. P. M. Danehy, S. O, Byrne, A. F. P. Houwing, J. S. Fox, and D. R. Smith, "Flow-tagging velocimetry for hypersonic flows using fluorescence of nitric oxide," AIAA Journal **41**, 263-271 (2003).

31. R. K. Hanson, "Planar laser-induced fluorescence imaging," J. Quant. Spectrosc. Radiat. Transfer **40**, 343-362 (1988).

32. R. N. Zare, "My life with LIF: A personal account of developing laser-induced fluorescence," Annu. Rev. Anal. Chem. **5**, 1-14 (2012).

33. G. Herzberg, *Molecular Spectra and Molecular Structure*, Spectra of Diatomic Molecules (D. Van Nostrand Company Inc., 1955).

34. J. Danielak, U. Domin, R. Ke, M. Rytel, and M. Zachwieja, "Reinvestigation of the emission γ band system ($A\ ^2\Sigma^+$–$X\ ^2\Pi$) of the NO molecule," J. Mol. Spectrosc. **181**, 394-402 (1997).

35. J. Luque and D. R. Crosley, "LIFBASE: Database and spectral simulation program (version 1.5)," SRI International Report MP 99-009 (SRI, 1999).

36. J. F. Burris, T. J. McGee, and J. Barnes, "Time-resolved fluorescence studies of the $A\ ^2\Sigma^+$ (v' = 1) state of nitric oxide: Lifetimes and collisional deactivation rates," Chem. Phys. Letters **121**, 371-376 (1985).

37. J. Anderson, "Oblique shock and expansion waves," in *Modern Compressible Flow: With Historical Perspective,* 3 edition ed. (McGraw-Hill Education, 2003).

38. D. B. Atkinson and M. A. Smith, "Design and characterization of pulsed uniform supersonic expansions for chemical applications," Rev. Sci. Instrum. **66**, 4434-4446 (1995).

39. B. F. Bathel, P. M. Danehy, J. A. Inman, S. B. Jones, C. B. Ivey, and C. P. Goyne, "Velocity profile measurements in hypersonic flows using sequentially imaged fluorescence-based molecular tagging," AIAA Journal **49**, 1883-1896 (2011).

40. B. Brett, D. Paul, I. Jennifer, J. Stephen, I. Christopher, and G. Christopher, "Multiple velocity profile measurements in hypersonic flows using sequentially-imaged fluorescence tagging," in *48th AIAA Aerospace Sciences Meeting Including the New Horizons Forum and Aerospace Exposition* (American Institute of Aeronautics and Astronautics, 2010).

41. M. Hunter, S. A. Reid, D. C. Robie, and H. Reisler, "The monoenergetic unimolecular reaction of expansion-cooled NO_2: NO product state distributions at excess energies 0–3000 cm^{-1}," J. Chem. Phys. **99**, 1093-1108 (1993).

42. M. D. Lahr, R. W. Pitz, Z. W. Douglas, and C. D. Carter, "Hydroxyl-tagging-velocimetry measurements of a supersonic flow over a cavity," J. Propulsion. Power **26**, 790-797 (2010).

43. L. A. Ribarov, J. A. Wehrmeyer, S. Hu, and R. W. Pitz, "Multiline hydroxyl tagging velocimetry measurements in reacting and nonreacting experimental flows," Exp. Fluids **37**, 65-74 (2004).

44. G. Hancock and M. Saunders, "Vibrational distribution in NO (X $^2\Pi$) formed by self quenching of NO A $^2\Sigma^+$ (v = 0)," Phys. Chem. Chem. Phys. **10**, 2014-2019 (2008).

45. M. A. Burgos Paci, J. Few, S. Gowrie, and G. Hancock, "Products of the quenching of NO A $^2\Sigma^+$ (v = 0) by N_2O and CO_2," Phys. Chem. Chem. Phys. **15**, 2554-2564 (2013).

46. T. B. Settersten, B. D. Patterson, H. Kronemayer, V. Sick, C. Schulz, and J. W. Daily, "Branching ratios for quenching of nitric oxide A $^2\Sigma^+$ (v′ = 0) to X $^2\Pi$ (v" = 0)," Phys. Chem. Chem. Phys. **8**, 5328-5338 (2006).

47. M. P. Lee, B. K. McMillin, and R. K. Hanson, "Temperature measurements in gases by use of planar laser-inducedfluorescence imaging of NO," Appl. Opt. **32**, 5379-5396 (1993).

48. B. K. McMillin, M. P. Lee, and R. K. Hanson, "Planar laser-induced fluorescence imaging of shock-tube flows with vibrational nonequilibrium," AIAA Journal **30**, 436-443 (1992).

49. T. B. Settersten, B. D. Patterson, and W. H. Humphries, "Radiative lifetimes of NO A $^2\Sigma^+$ (v′ = 0, 1, 2) and the electronic transition moment of the A $^2\Sigma^+$−X $^2\Pi$ system," J. Chem. Phys. **131**, 104309 (2009).

50. R. Sánchez-González, W. D. Eveland, N. A. West, C. L. N. Mai, R. D. W. Bowersox, and S. W. North, "Low-temperature collisional quenching of NO A $^2\Sigma^+$ (v′ = 0) by NO (X $^2\Pi$) and O_2 between 34 and 109 K," J. Chem. Phys. **141**, 074313 (2014).

51. T. Ebata, Y. Anezaki, M. Fujii, N. Mikami, and M. Ito, "Rotational energy transfer in NO (A $^2\Sigma^+$, v = 0 and 1) studied by two-color double-resonance spectroscopy," Chem. Phys. **84**, 151-157 (1984).